



HAL
open science

Modelling of thermal conductivity and nonlinear mechanical behavior of straw insulation composite by a numerical homogenization approach

Brahim Ismail, Naïma Belayachi, Dashnor Hoxha, Laurent Arbaret

► To cite this version:

Brahim Ismail, Naïma Belayachi, Dashnor Hoxha, Laurent Arbaret. Modelling of thermal conductivity and nonlinear mechanical behavior of straw insulation composite by a numerical homogenization approach. *Journal of Building Engineering*, 2021, pp.103144. 10.1016/j.job.2021.103144 . insu-03329634

HAL Id: insu-03329634

<https://insu.hal.science/insu-03329634>

Submitted on 31 Aug 2021

HAL is a multi-disciplinary open access archive for the deposit and dissemination of scientific research documents, whether they are published or not. The documents may come from teaching and research institutions in France or abroad, or from public or private research centers.

L'archive ouverte pluridisciplinaire **HAL**, est destinée au dépôt et à la diffusion de documents scientifiques de niveau recherche, publiés ou non, émanant des établissements d'enseignement et de recherche français ou étrangers, des laboratoires publics ou privés.

Journal Pre-proof

Modelling of thermal conductivity and nonlinear mechanical behavior of straw insulation composite by a numerical homogenization approach

Brahim Ismail, Naima Belayachi, Dashnor Hoxha, Laurent Arbaret



PII: S2352-7102(21)01002-0

DOI: <https://doi.org/10.1016/j.jobe.2021.103144>

Reference: JOBE 103144

To appear in: *Journal of Building Engineering*

Received Date: 30 March 2021

Revised Date: 29 July 2021

Accepted Date: 14 August 2021

Please cite this article as: B. Ismail, N. Belayachi, D. Hoxha, L. Arbaret, Modelling of thermal conductivity and nonlinear mechanical behavior of straw insulation composite by a numerical homogenization approach, *Journal of Building Engineering* (2021), doi: <https://doi.org/10.1016/j.jobe.2021.103144>.

This is a PDF file of an article that has undergone enhancements after acceptance, such as the addition of a cover page and metadata, and formatting for readability, but it is not yet the definitive version of record. This version will undergo additional copyediting, typesetting and review before it is published in its final form, but we are providing this version to give early visibility of the article. Please note that, during the production process, errors may be discovered which could affect the content, and all legal disclaimers that apply to the journal pertain.

© 2021 Published by Elsevier Ltd.

Modelling of thermal conductivity and nonlinear mechanical behavior of straw insulation composite by a numerical homogenization approach

Brahim ISMAIL¹, Naima BELAYACHI¹, Dashnor HOXHA¹, Laurent ARBARET²

¹ Université d'Orléans, INSA Centre Val de Loire, Université de Tours, Laboratoire de Mécanique Gabriel Lamé Polytech Orléans, 8 rue Léonard de Vinci, 45072 Orléans, France

² ISTO, UMR 7327, Université d'Orléans, CNRS, BRGM, 1A rue de la Férellerie, 45071, Orléans, France

Corresponding author :

Naima Belayachi

Tel : 330238492502

Fax : 330238417063

E-mail address : naima.belayachi@univ-orleans.fr

Postal address : Laboratoire LaMé, Polytech'Orléans

8 Rue Léonard De Vinci

45072, Orléans cedex 2, France

Highlights

- Thermal conductivity and mechanical behavior of new straw composite were modeled using 3D numerical homogenization.
- X-ray micro-tomography was used to determine volume fractions of composite constituents.
- A particular shape of inclusion “3D-curved spherocylindrical” was adopted to represent plant aggregates.
- The numerical homogenization method used, allowed to predict the mechanical strength of the new bio-based composite.

31

32

33 Abstract

34 Bio-based materials have been extensively studied in recent decades. These materials based
35 on vegetable aggregates are highly heterogeneous, and their complex behaviour depends on
36 the behaviour of the constituents as well as their spatial distribution, size, and shape.
37 Classically, homogenization methods are used for the prediction of the behaviour of
38 heterogeneous materials because they allow to take into-account the microscopic phenomena
39 and characteristics governing the macroscopic behaviour at a considered scale. In the case of
40 composite materials, the use of this prediction approach allows to optimize the properties
41 according to some criteria while limiting often expensive and time-consuming experimental
42 tests. This paper aims to predict the effective thermal conductivity and model the mechanical
43 behaviour of a bio-composite based on lime and cereal straw. A numerical homogenization
44 approach was adopted to consider the complex microstructure of these biobased materials. An
45 experimental characterization of the composites was carried out to describe the microstructure
46 of the material (size, orientations, and shape of aggregates). X-Ray micro tomography
47 observation was performed to determine volume fraction of the different phases of the
48 biocomposite.

49 A statistical approach was also used to determine the size of the Representative Volume
50 Element (RVE) of the studied material for different distributions of heterogeneities. Then,
51 numerical simulations of the thermal and mechanical behavior of composite was carried out.
52 The results show the need to take into account an interphase between the straw aggregates and
53 the matrix as well as the effect of the vegetal aggregates on the hydration of the binder to
54 accurately predict the effective properties of the material.

55 **Keywords:** Straw Composite, Thermal Conductivity, Mechanical Behavior, X-Ray Micro-
56 tomography, Representative Volume Element (RVE), Modeling, Numerical Homogenization,

57 **1 Introduction**

58 Bio-based materials have a growing interest in improving building thermal performance and
59 reduces the carbon emissions of the construction sector. Generally, these materials are based
60 on vegetable, renewable aggregates and organic/inorganic binders [1–7]. Numerous scientific
61 studies have been carried out on the development and the experimental characterization of
62 these composites. They showed interesting thermal, acoustic insulation capacities and
63 excellent hydric properties of these materials [8–14] combined with interesting characteristics
64 such as low energy consumption, low carbon footprint, low cost, low density and
65 biodegradability [15–19]. The properties of the bio-composites depend strongly on the
66 fraction and the morphology of the constituents, in particular the type and content of binder,
67 the distribution and the size of the aggregates [20,21]. It has also been reported in the
68 literature that the relative humidity significantly impacts the thermal conductivity of the
69 composites due to their hygroscopic nature [22–24].

70 Several works in the literature have attempted to determine thermal and mechanical
71 macroscopic properties of this type of materials by taking into account their microstructure
72 [22, 24–27]. In all these works self-consistent homogenization based on a spherical inclusion
73 (bicomposite or tricomposite) was used. However, the predictions of this method become
74 medicor when the binder fraction decreases below 19% of the volume because of the
75 assumption of the matrix continuity which is not verified for this case [25]. Akkaoui et al.
76 2017 [28] have used self-consistent method combined with a composite-sphere like
77 microstructure to predict the Young modulus of a wood aggregate concrete. Following these
78 authors the representation of the microstructure of wood concrete as an aggregation of solid
79 grains surrounded by a layer of binder and porosity represented by voids among these

80 aggregates seems to be a better alternative of structure description as compared to hollow
81 spherical inclusions microstructure used by [25]. The results obtained, using this
82 microstructure representation are in good agreement with the experimental measurements and
83 model has been considered according to the authors as a predictive tool to optimize the elastic
84 properties of wood aggregate concrete [28]. However, the use of such microstructure
85 representation remains limited to the case of materials with an intergranular porosity of less
86 than 50% which is the percolation limit of the self-consistent scheme.

87 In a recent study, Tran-Le et al. 2018 [29] have developed a novel analytical model approach
88 to predict effective thermal conductivity tensor of lime-hemp concrete by taking into account
89 the anisotropy, size, orientation of aggregates and the interface between the binder and
90 aggregates. This approach could be seen as an extension of the Eshelby's solution to several
91 ellipsoidal inclusions. By comparing results of their model with experimental measures, they
92 concluded on the necessity of taking into account in modeling the thermal contact resistance
93 between the aggregates and the binder, in order to fit the observed values of thermal
94 conductivity. This model constitutes a suitable prediction tool of the thermal conductivity of
95 hemp concrete, but it is only valid in the dry state.

96 Couture et al. 2017 [30] also noted that the pre-compaction used during the manufacturing of
97 the materials leads to anisotropy of thermal conductivity at the macroscopic scale. The
98 authors adopted a numerical approach based on finite element calculations to model the
99 thermal conductivity of hemp concrete. The hemp aggregates were represented by cylindrical
100 inclusions aligned in the same direction and arranged randomly. However, their volume
101 fraction does not exceed 15%. The authors confirmed by the simulations carried out, the
102 transverse isotropic character of thermal conductivity of hemp concrete. Mom et al. 2011 [31]
103 used an iterative homogenization approach based on finite element calculations to model the
104 thermal conductivity of hemp concrete with bar shaped particles and high porosity rates. This

105 approach made it possible to take into account the anisotropy of the material and to represent
106 the hemp particles by plate inclusion. The authors compared the results of this model with the
107 experimental measurements of Cerezo 2005 [25] and Nguyen et al. 2018 [32]. They
108 concluded that the multi-scale iterative technique adopted, provides a satisfactory prediction
109 of thermal conductivity.

110 The knowledge of the effective properties of other lightweight insulation materials is also a
111 topic of actual interest of foam concretes, due to their wide use in construction project. This
112 special class of porous materials with cellular microstructure have been extensively studied by
113 using periodic homogenization method. Low et al 2020 [33] studied the influence of
114 boundary conditions on the computation of the effective thermal conductivity of foams with a
115 high porosity of 74%. Three types of foam geometries were used, namely, unit cell-based
116 structures, digitally generated periodic foams, and tomography-reconstructed real foams. The
117 authors have shown the importance of choosing the appropriate boundary conditions for the
118 geometries used to accurately estimate the effective thermal conductivity. Miled et al 2016
119 [34] proposed a three dimensional finite Element Method for the prediction of the effective
120 thermal conductivity of foam concretes having a porosity ranging between 0 and 0.68. They
121 have reported that the effective thermal conductivity of foam concretes can be predicted
122 according to their porosity by a general power law. Their results also showed no significant
123 effect of the pores size distribution, and spatial distribution on the effective thermal
124 conductivity of foam concretes.

125 The present study aims to predict the thermal conductivity and model mechanical behavior of
126 straw insulation composite developed in previous works by authors [2,35]. The objective is
127 the mixtures optimization by using predictive capacity of homogenization approach in order
128 to limit experimental tests. A numerical homogenization approach is adopted to take into
129 account a complex microstructure more representative of the real composite, considering the

130 size, the shape, the orientation of the aggregates with high rate and also the
 131 significant intergranular porosity. In addition to Young's modulus prediction of biobased
 132 concrete, a subject very often treated in abundant research, the modeling approach proposed
 133 aims at description of full nonlinear mechanical behavior of this biocomposite. In fact, the
 134 mechanical strength in compression is an essential parameter to be determined for all
 135 constructing materials. So, the proposed non-linear modeling should be a tool to estimate the
 136 mechanical strength of straw concrete as a function of the structure and composition. Using
 137 the model makes it possible to optimize the mixtures by taking into account two criteria of
 138 use, a better thermal performance and a good mechanical strength for material's buildability.

139 2 Materials and characterization methods

140

141 2.1 Materials

142

143 Two composites were selected from previous work [35] for this investigation. The first is
 144 based on lime with a ratio of Water/Binder = 1.1 and Straw/Binder = 0.2 and the second
 145 prepared with the same Water/Binder ratio and a higher ratio of Straw/Binder = 0.4 with a
 146 binder consisting of lime and 20 % gelatin. The use of this biopolymer allows increasing of
 147 the ratio of vegetal aggregates. The description of raw materials and manufacturing procedure
 148 is detailed in the work of Ismail et al. 2020 [35]. The composites are denoted respectively C1
 149 and C2, as indicated in Tab. 1.

Composites	Binder	Straw/Binder (kg/kg)	Water/Binder (kg/kg)	Density (kg/m ³)
C1	Lime	0.2	1.1	450
C2	Lime+20% gelatin	0.4	1.1	300

150 **Tab. 1.** Composite designation and detailed mixture proportions

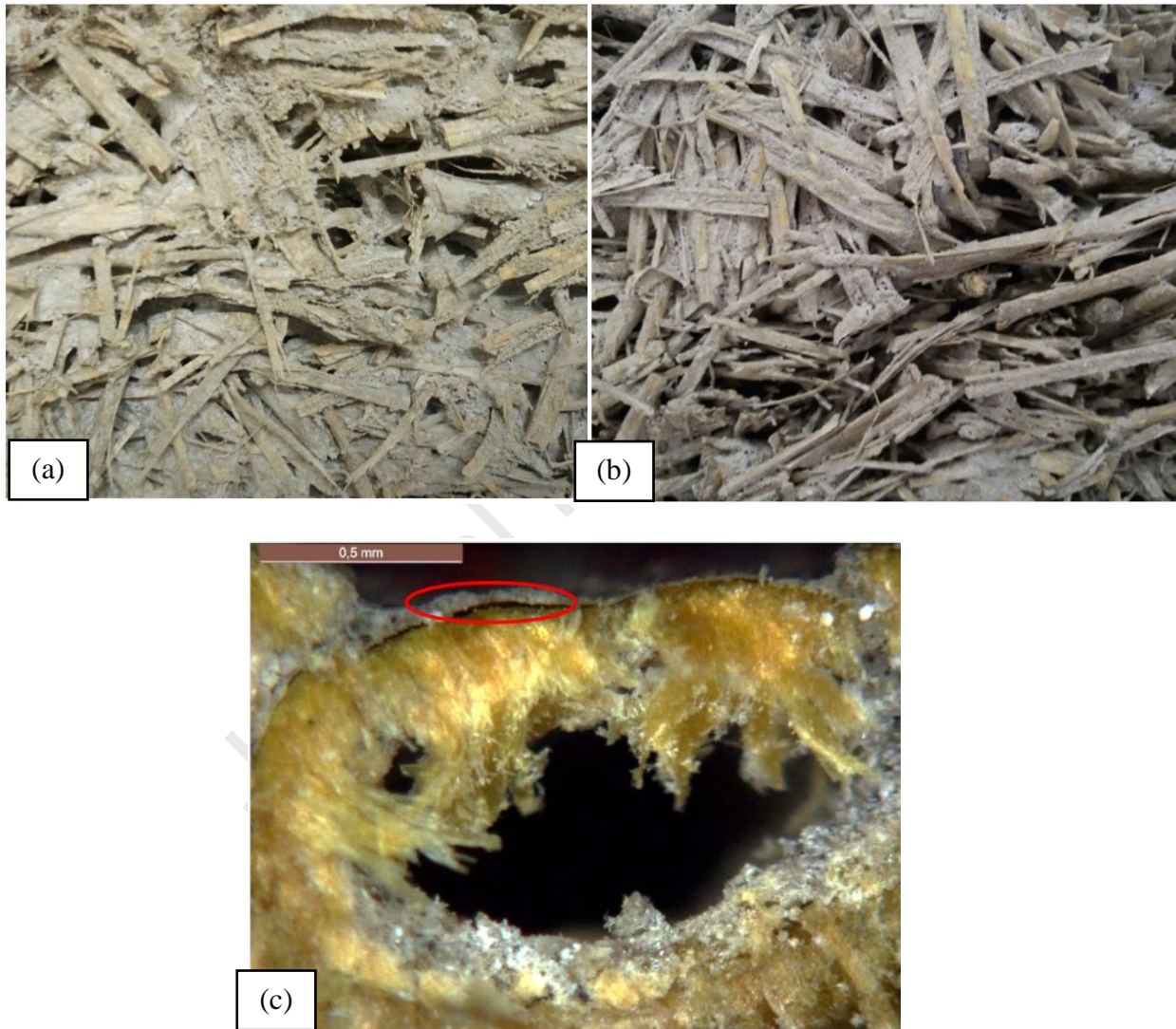
151

152 Fig. 1 shows the appearance of the two composites. We can observe that in both cases, the
 153 aggregates are coated with a layer of binder and voids between them. These coated aggregates

154 are connected by binder bridges. There are randomly arranged and not always straight but are
155 curved due to their low stiffness. We can also observe in Fig 1c the presence of the interphase
156 or decohesion between the straw aggregate and the matrix.

157

158



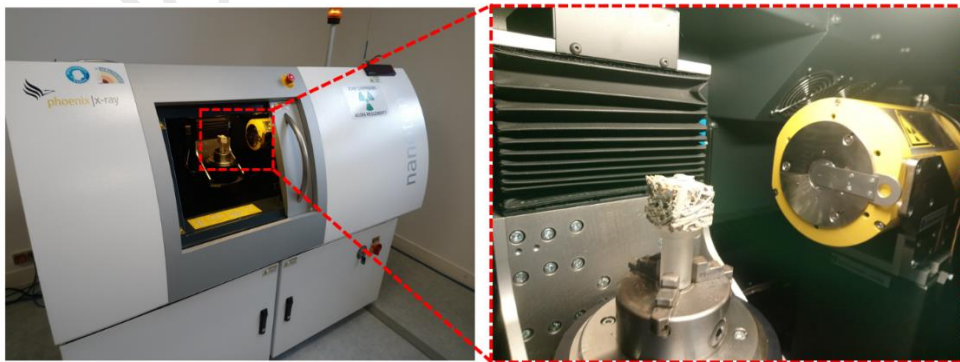
159

160 **Fig. 1.** Appearance of composites (a) C1 (with a high binder content) (b) C2 (with a low
161 binder content) (c) microscope visualization of the straw aggregate–matrix interface

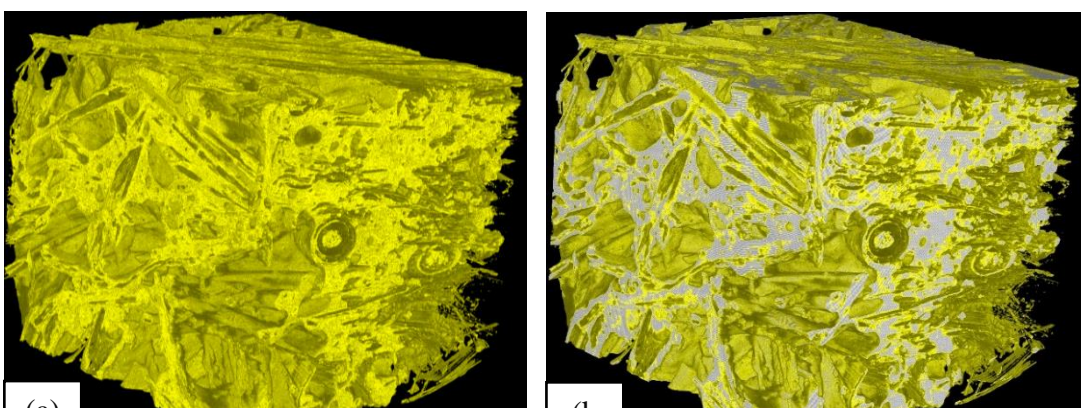
162 2.2 Experimental characterization

163 2.2.1 X-ray micro-tomography: volume fractions of the constituents:

164 In order to determine the fraction of each constituent phase in composites, micro computed
 165 tomography (microCT) analyses were performed at the Institut des Sciences de la Terre
 166 d'Orléans (Orléans, France) on a Nanotom 180NF from Phoenix X-Ray (Fig. 2). We used an
 167 accelerating voltage of 180 kV, a filament current of 170 nA, and an operating voltage of 120
 168 V. During acquisition, the sample rotates 360°, allowing the instrument to take successive
 169 images, covering all angles. Microtomography analysis was performed on representative
 170 samples of $3 \times 3 \times 3 \text{ cm}^3$ which resulted in a resolution of $17 \mu\text{m}^3$ per voxel. After the
 171 analysis, the stack of 2D images is processed to construct a volume, manually extracted using
 172 the software VG-Studio Max 1.2. A 3^3 median filter was applied to obtain homogeneous and
 173 clear images. The dataset was processed by VGStudio MAX software. Fig. 3 shows an
 174 example of 3D-reconstruction images obtained for the C1 composite. Tab. 2 shows the
 175 volume fractions of the constituents obtained for the two composites, C1 (with a high binder
 176 content) and C2 (with a low binder content).



177
 178 **Fig. 2.** Nanotom tomograph with a straw composite sample



183
184
185
186
187
188
189
190
191
192
193
194
195
196
197

Fig. 3. 3D-reconstruction of a straw concrete sample (a) straw (b) combination straw and binder (c) composite (straw+binder+porosity).

	C1	C2
Binder	33%	11%
Straw	30%	35%
Porosity (intergranular)	37%	54%

198
199

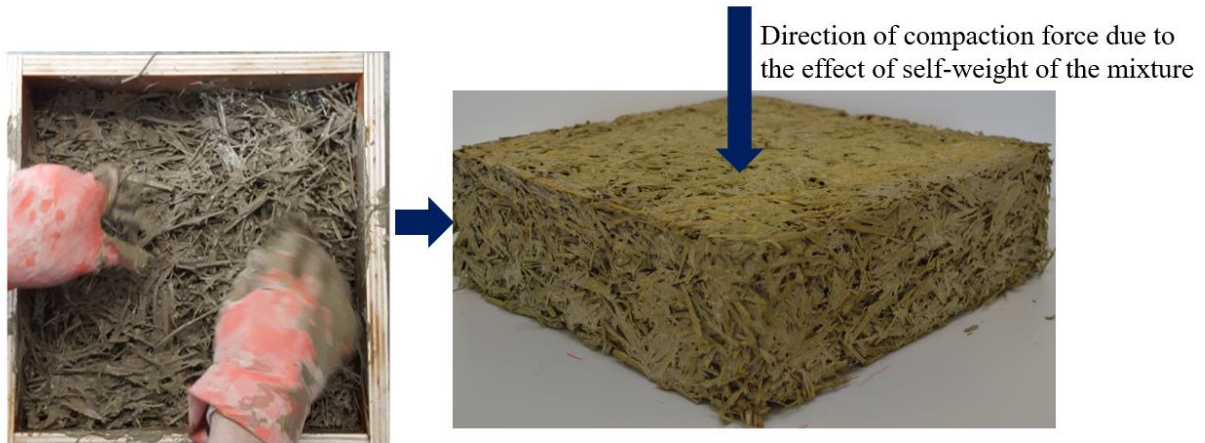
Tab. 2 . Volume fractions of the different phases for the two composites

200 2.2.2 Thermal and mechanical characterization

201 To evaluate the experimental mechanical behavior of the two composites, uniaxial
202 compression tests were carried out using a compression testing machine (IGM250), equipped
203 with a load cell of 25 kN at a displacement rate of 0.5 mm/min. It should be noted that during
204 the manufacture of composites, under the effect of the self-weight of the mixture, the straw
205 aggregates tend towards stratified planes perpendicular to the compaction direction (Fig. 4).
206 For this reason, the tests were carried out in the perpendicular direction to compaction
207 (horizontal) on $20 \times 20 \times 10 \text{ cm}^3$ samples (Fig. 5-a) and also in the parallel direction of
208 aggregates (vertical) on $15 \times 15 \times 10 \text{ cm}^3$ samples (Fig. 5-b).

209

210



211

212 **Fig. 4.** Direction of compaction due to the self-weight of the mixture

213

214

215

216

217

218

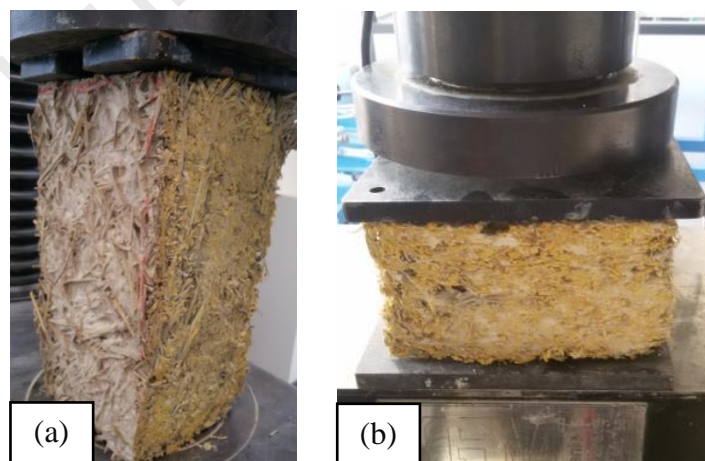
219

220

221

222

223



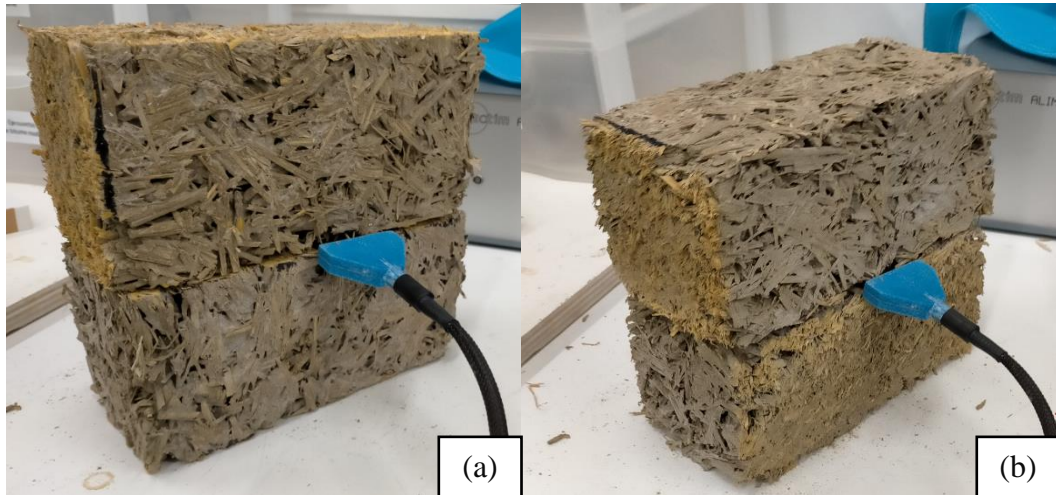
224 **Fig. 5.** Uniaxial compression test (a) horizontal direction (b) vertical direction

225 Thermal conductivity was measured using a NeoTIM conductivity meter based on the hot

226 wire technique. The measurements were made on samples with the dimensions 20 cm × 10

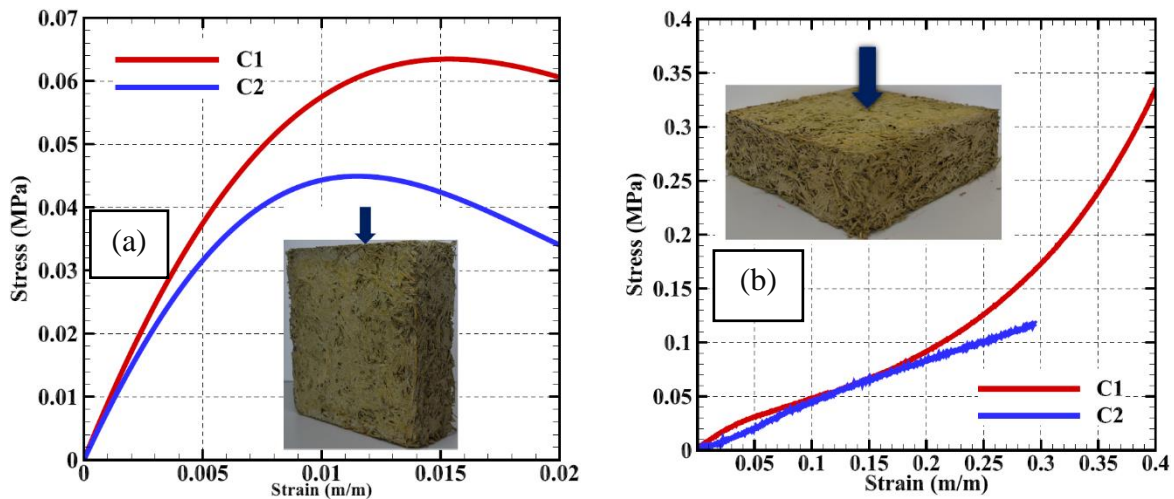
227 cm × 10 cm in horizontal (Fig. 6a) and vertical direction (Fig. 6b). The probe was placed in

228 five different positions and the test was repeated three times in each position. The test was
229 carried out in a dry state (the composites were dried in a ventilated oven at 60 °C until mass
230 stabilization).



231

232 **Fig. 6.** Thermal conductivity measurement (a) horizontal direction (b) vertical direction.
233 The thermal and mechanical characterization carried out in the horizontal and vertical
234 direction highlighted the effect of the aggregate's orientation on the behavior of the materials.
235 Fig. 7 shows a comparison between the stress-strain curves evaluated from the uniaxial
236 compression tests on the composites studied in both directions. The mechanical behaviour
237 obtained in the horizontal direction is similar to what is observed for hemp concrete [36]. The
238 curve has three zones: an elastic zone, where the binder supports the compressive stress, a
239 nonlinear zone depicting the progressive cracking of the binder until failure, and a post peak
240 zone where the binder is totally damaged and the vegetal aggregate supports most of the
241 stresses. Contrary to the horizontal direction, the loading of the composites in the vertical
242 direction results a behavior which is characterized by the absence of a fracture peak (Fig.7b),
243 the curve shows a continuous compaction with increase of the stress with large strain.



244 **Fig.7 .** Mechanical behavior of composites (a) horizontal direction (b) vertical direction.

245 A difference in thermal conductivity was also noted in both directions. The values measured
 246 in the vertical direction are higher than those obtained in the horizontal direction for both
 247 composites as presented in Tab.3.

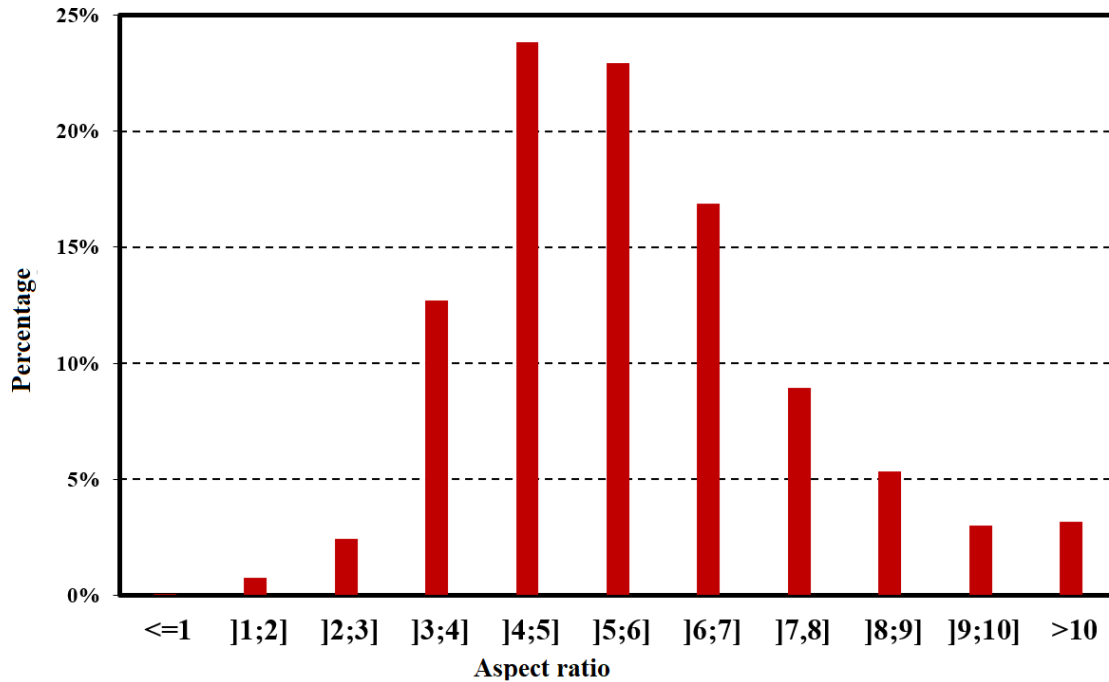
248 These results show that the fibre orientation strongly influences the properties of the
 249 composites and leads to a transverse isotropy of the materials [30].

Composites	Thermal conductivity ($\lambda/W/m.K$)	
	Vertical direction	Horizontal direction
C1	0.075 ± 0.02	0.064 ± 0.013
C2	0.057 ± 0.017	0.051 ± 0.019

250 **Tab.3 .** Thermal conductivity of composites in horizontal and vertical direction

251 2.2.3 Distribution of fiber aspect ratio

252 Fig.8 show the results of the distribution of fiber aspect ratio obtained from the granulometric
 253 analysis of aggregates [35], it can be seen that more than 75% of the aggregates have an
 254 aspect ratio in the range of 3-7, with the largest percentage being assigned to aspect ratio in
 255 the interval]4 ;5].

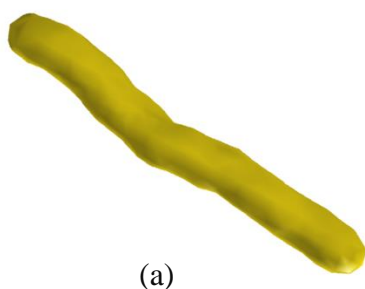


256

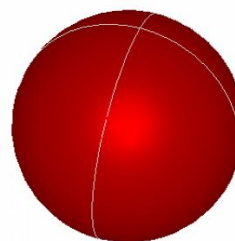
257 **Fig. 8.** Distribution of aspect ratio of aggregates used for the manufacture of composites.258 **3 Modeling of thermal conductivity and nonlinear mechanical behavior**259 **3.1 Conceptual model of the microstructure of the biocomposites**

260

261 The microstructural information obtained from the experimental characterization described in
 262 the previous section was used to create a three-dimensional microstructure using the Digimat
 263 software. The straw aggregates were represented by curved sphero-cylindrical inclusions (Fig.
 264 9a) with a constant aspect ratio equal to 4 and the porosity (intergranular porosity or straw
 265 porosity) was represented by spherical inclusions (Fig. 9b) randomly distributed. Also, in
 266 order to take into account the anisotropy demonstrated in previous section, the sphero-
 267 cylindrical inclusions were randomly oriented in the plane (2D) (Fig. 10).



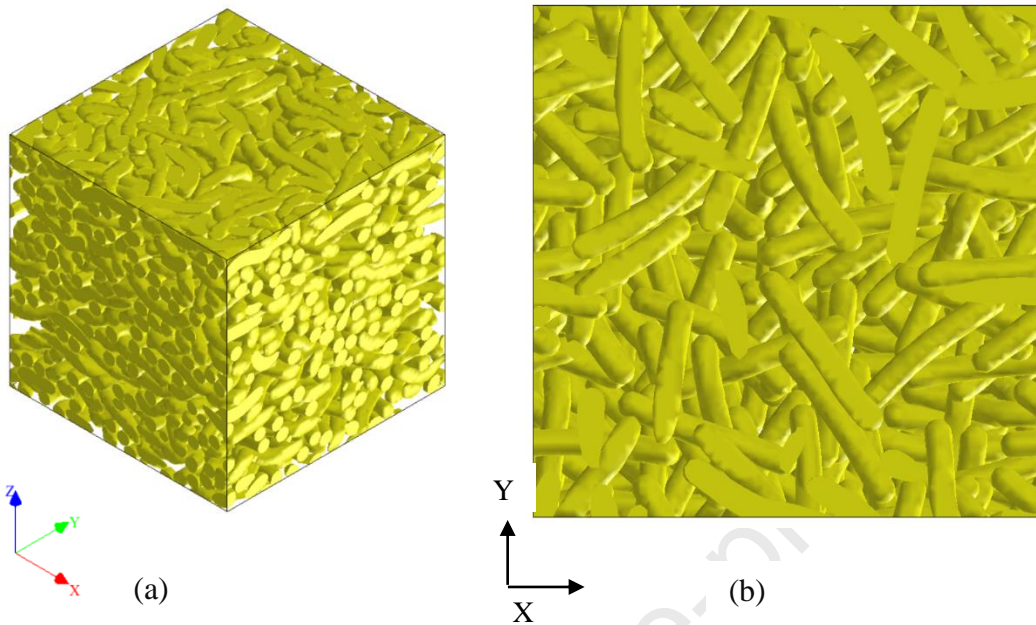
(a)



(b)

268

269

Fig. 9. Shapes of inclusion adopted for (a) straw (b) Porosity

270

271

Fig. 10. Example of a RVE showing the random orientation in the plane of inclusions.

272

273

274

In order to highlight the influence of the microstructure on the effective thermal conductivity of the biocomposites, five different configurations of the conceptual model of the biocomposite microstructure have been adopted:

275

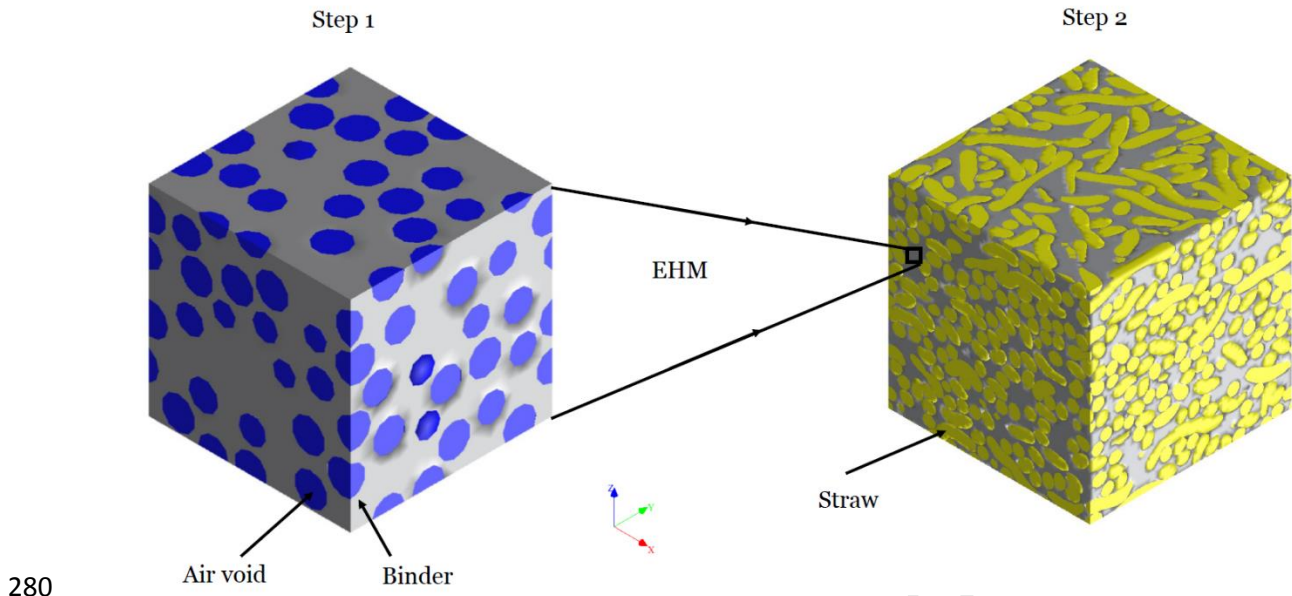
276

277

278

279

Configuration 1: It consists of introducing the heterogeneities of the material in two successive steps. First, the binder and porosity were homogenized. Then, the obtained equivalent homogeneous medium (EHM), constituted the matrix in the second step, while the straw inclusions were integrated to determine the effective conductivity of the final homogenized material (Fig. 11).



280

281

Fig. 11. Microstructure used in configuration 1

282

Configuration 2: The binder has been divided into two parts: a large part (95%) that coats the fibers and another part (5%) that provides the bonding bridges (porous binder) between them.

283

Therefore, the heterogeneities were represented by a tri-composite inclusion containing the air surrounded by the straw and itself coated with the layer of binder. Then, a two-step

284

homogenization was also adopted: the first step consists in determining separately the

285

effective thermal conductivity of the tri-composite inclusion (air + straw + binder) and the

286

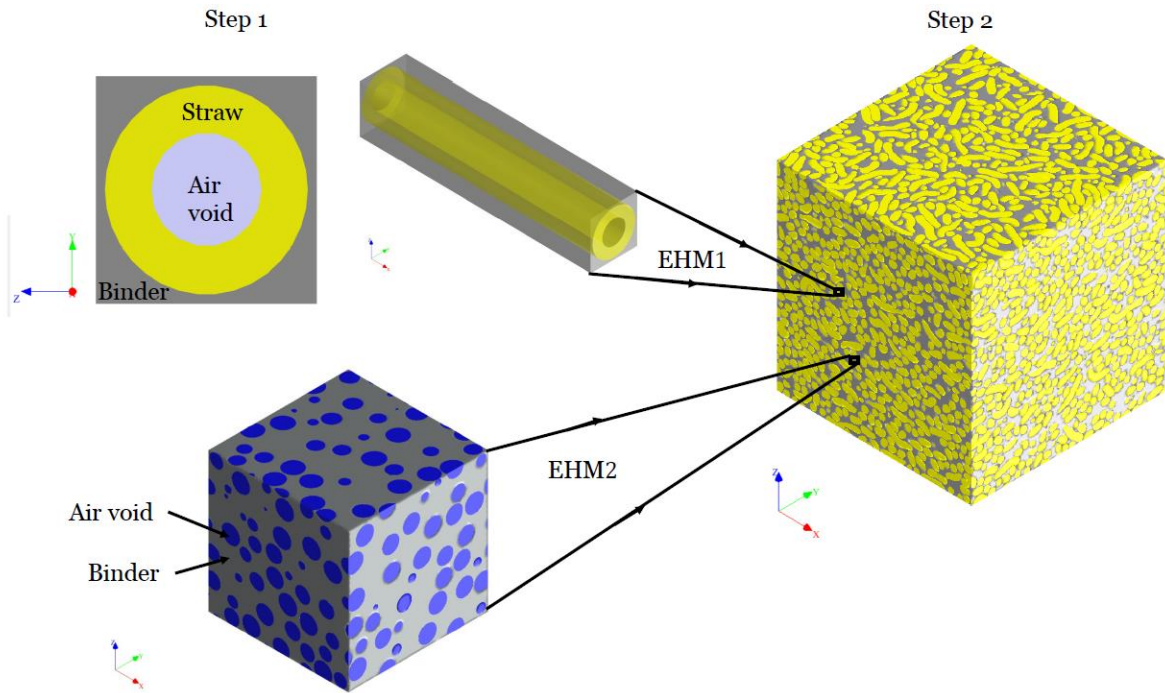
porous binder. Then for the second step, the RVE contain the two homogeneous media

287

determined in the first one to obtain the final effective behavior (Fig. 12).

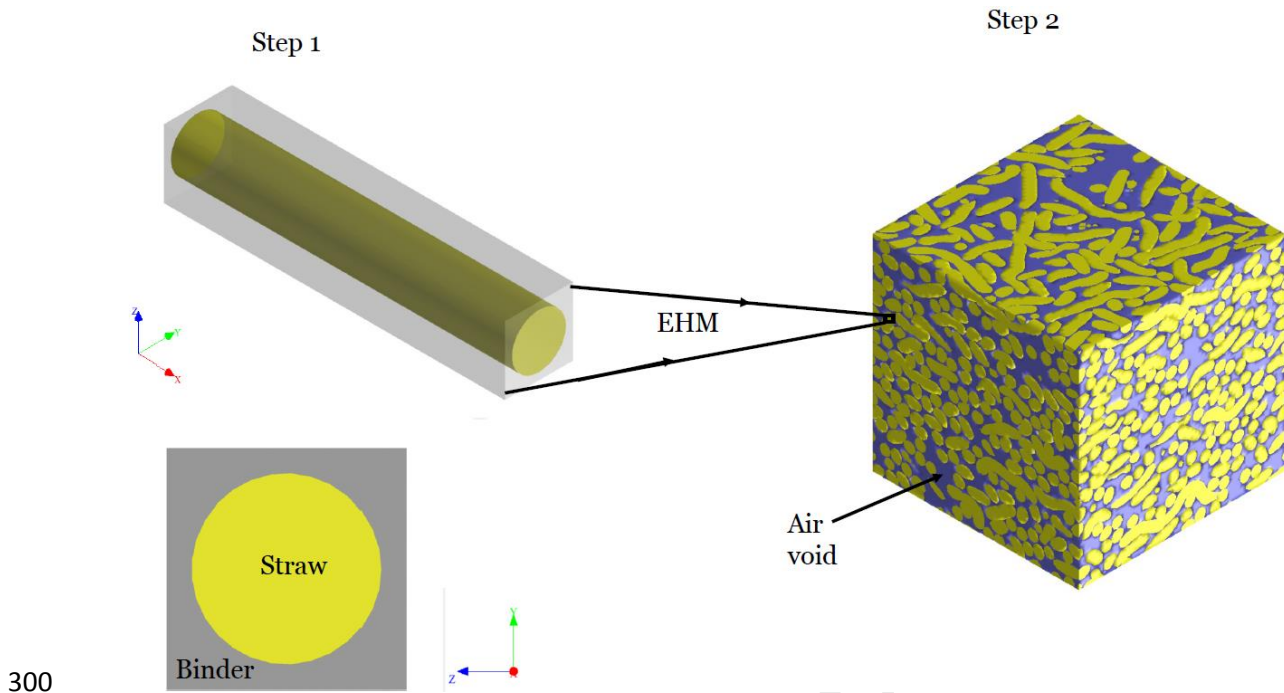
288

289



290
 291 **Fig. 12.** Microstructure used in configuration 2
 292

293 Configuration 3: we assume in this case that the material consists of a network of fibers
 294 coated by the binder and embedded in the void matrix. The process consists in a first step in
 295 determining the effective thermal conductivity of a bi-composite inclusion representing the
 296 straw coated by the binder. Then, this conductivity will be assigned to heterogeneities
 297 immersed in a matrix completely represented as a void and a second homogenization was
 298 carried out. Note that the contact between the binder and the straw is considered as perfect
 299 (Fig. 13).

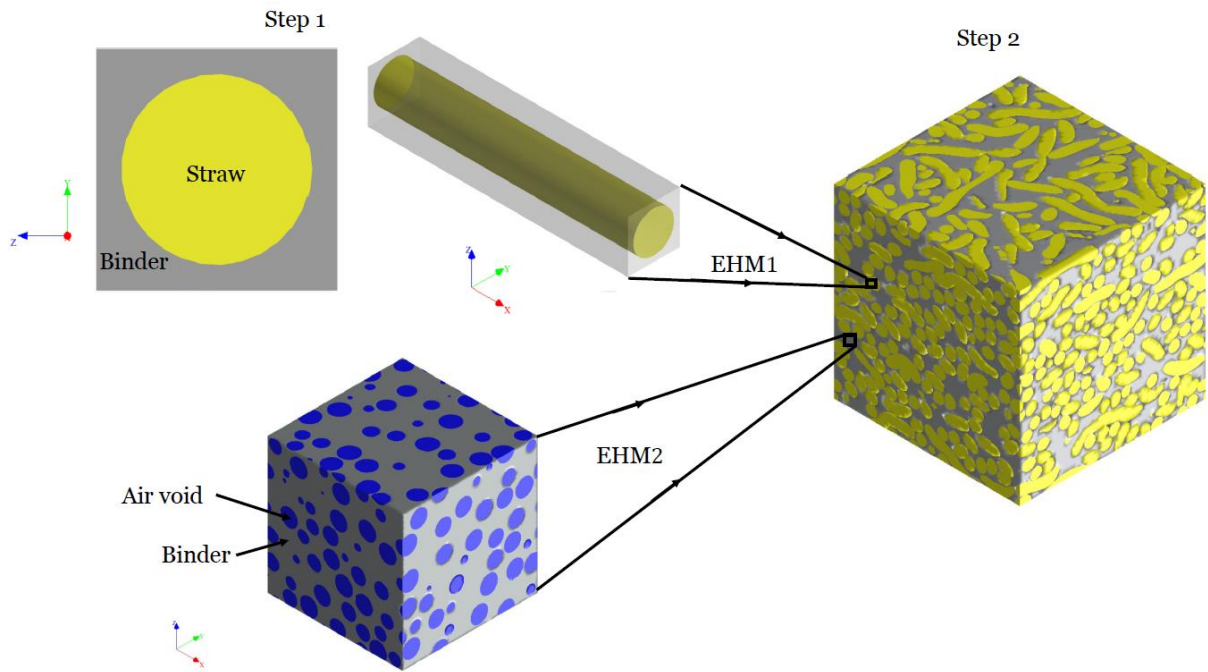


300

301

Fig. 13. Microstructure used in configuration 3

302 Configuration 4: Similar to the second configuration, the binder was divided into two parts, a
 303 95% percentage that coats the fibers and another 5% which connects the fibers with each
 304 other. In a first step, the equivalent homogeneous medium of the bi-composite inclusion and
 305 the porous binder were determined, then in a second step, the two equivalent homogeneous
 306 mediums were integrated in an RVE where the matrix represents the porous binder and the
 307 heterogeneities represent the coated straw. A perfect interface was also considered in this case
 308 (Fig. 14).



309

310

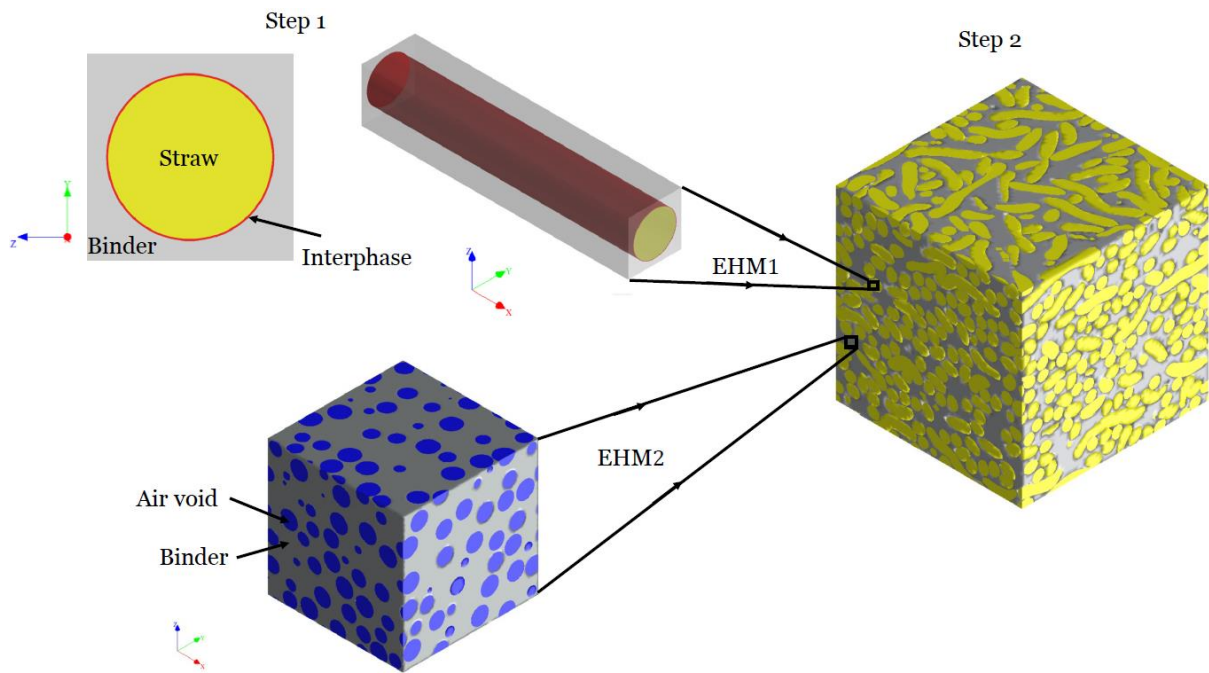
Fig. 14. Microstructure used in configuration 4

311 Configuration 5: The same previous approach was followed in this configuration but an inter-
 312 phase between binder and straw was introduced. The properties of this zone were determined
 313 by calibrating the numerical model on the experimental results. As for its thickness, it is
 314 assumed to be very small compared to the diameter of inclusion (interphase thickness $\approx 1\%$ of
 315 diameter of inclusion) (Fig. 15).

316

317

318



319

320

Fig. 15. Microstructure used in configuration 5

3.2 Size of the representative Volume Element (RVE)

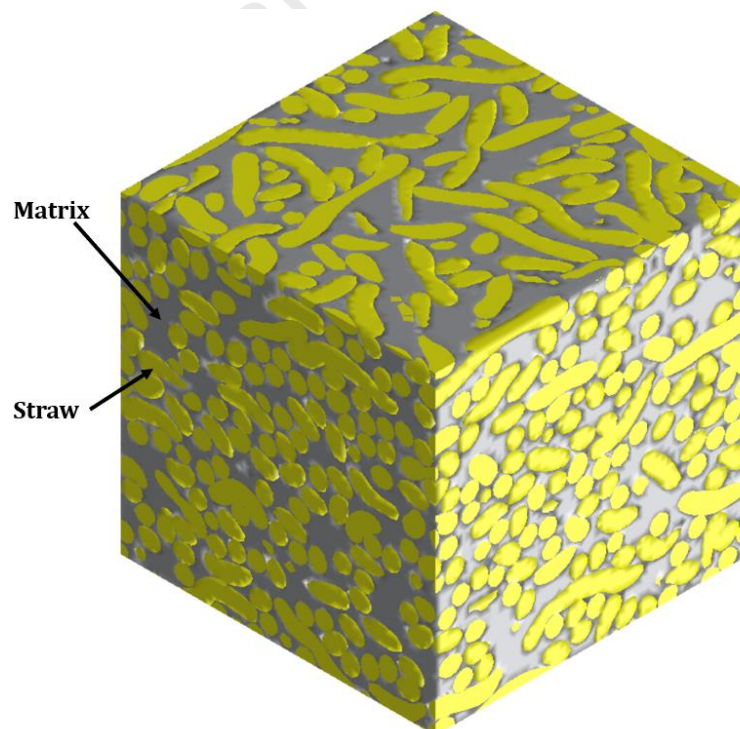
321

322

323 The relevant choice of a representative volume element (RVE) is the first step to accurately
 324 describe the microstructure of the material to be modelled. Several approaches have been
 325 proposed in the literature to determine its size. According to Hill.1963 [37], the RVE is a
 326 sample which contains sufficient heterogeneities for the macroscopic properties to be
 327 independent of the boundary conditions. Hashin.1983 [38] indicates that the RVE must be
 328 large enough in relation to the scale of the heterogeneity and small enough in relation to the
 329 macroscopic scale of the composite material. Kanit et al. 2003 [39], Gitman et al. 2007 [40],
 330 Pelissou et al. 2009 [41] proposed a statistical analysis based on the convergence of the
 331 effective properties to set the size of the representative volume. Indeed, the approach consists
 332 in estimating the apparent properties of the material by performing several numerical
 333 calculations on different sizes of the microstructure containing the same volume fraction of
 334 the heterogeneities and under the same boundary conditions. The size of the micro-structure

335 from which the apparent properties converge corresponds to the size of the Representative
336 Volume Element (RVE).

337 A similar approach is used here to determine the RVE size of straw composite in the thermal
338 and mechanical case. We consider five sizes of a cubic RVE whose dimension of the edge is
339 between 1 and 3 cm. We aim to determine for each size the effective thermal conductivity as
340 well as the Young's modulus. We also consider that the RVE contains a single form of
341 inclusion (curved sphero-cylindrical inclusions) with constant size and randomly oriented in
342 the plane (Fig.16). Five simulations were carried out for each size to determine the standard
343 deviation of the estimated parameters. The approach was applied for two volume fractions of
344 inclusions: 25% and 60%. The simulations and the generation of the microstructure were
345 carried out using the Digimat software. A set of parameters given in table 4, for lime matrix
346 and straw inclusion is used for all simulations.



347

348

Fig. 16. Microstructure used to determine the RVE size

349

350
351
352

	Matrix	Inclusion
Young's modulus E(MPa)	100	0.2
Poisson's ratio ν	0.3	0.1
Thermal conductivity (λ /W/m.K)	0.168	0.051

353

Tab. 4. Parameters used to determine effective properties.

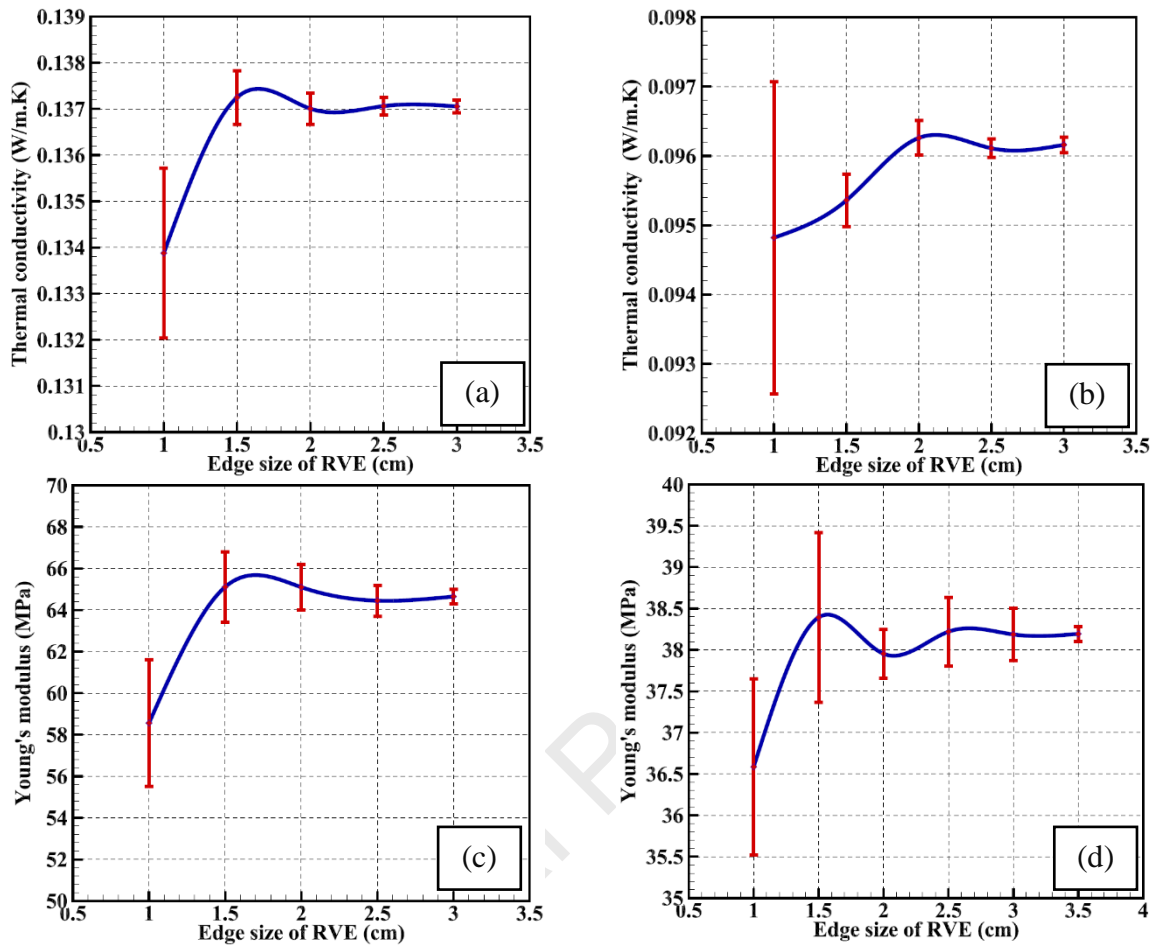
354 Fig. 17 shows the evolution of thermal conductivity and Young's modulus as a function of the
355 edge size of RVE for the two volume fractions considered. We can notice in the thermal case
356 that the effective conductivity converges from a size of 2 cm for a volume fraction of 25%
357 while for a fraction of 60% the convergence is shifted to a size of 2.5 cm.

358 In the case of Young's modulus, for a fraction of 25% the convergence was observed in the
359 vicinity of 2.5 cm while for a percentage of inclusions of 60%, it is reported at a size of 3 cm.
360 We can also note that in the different cases, the standard deviation decreases as the size of the
361 RVE increases.

362 These results show that the size of the RVE can depend on the volume fraction of the
363 heterogeneities in both linear elasticity and heat conduction. According to these results, a
364 representative cubic volume element with an edge of 3 cm was adopted to estimate the
365 thermal conductivity and the mechanical behavior of the studied straw composites. We note
366 that the average straw size is about 2.9 cm, determined from granulometric analysis of studied
367 particles [35]. However, to reduce the computation time of the simulations, we used in the
368 conceptual model of the microstructure an inclusion with an average size of about 1 cm which
369 allows to have a same ratio of 3 between the size of the inclusion and the RVE edge.

370
371

372



373 **Fig. 17.** Variations of the effective apparent properties as a function of the edge size of the
 374 RVE: (a) and (b) Thermal conductivity respectively for a fraction of 25 % and 60%; (c) and
 375 (d) Young's modulus respectively for a fraction of 25% and 60%

376 3.3 Modeling of thermal conductivity

377 As it was described above, we consider a cubic RVE with an edge of 3 cm, composed of a
 378 matrix and two types of inclusions: spherical representing the porosity (inter-granular and
 379 tubular pore of straw) and curved sphero-cylindrical corresponding to the vegetable
 380 aggregates. Tab. 5 shows the input data used for the three components. The thermal
 381 conductivities given for the matrices were measured on samples of the binder pastes using the
 382 hot wire method. The numerical simulations were performed using a Digimat software.
 383 A temperature difference of 20°C was imposed between two opposite hot and cold faces and
 384 periodicity boundary conditions on the other faces (Fig. 18). The thermal loading was applied

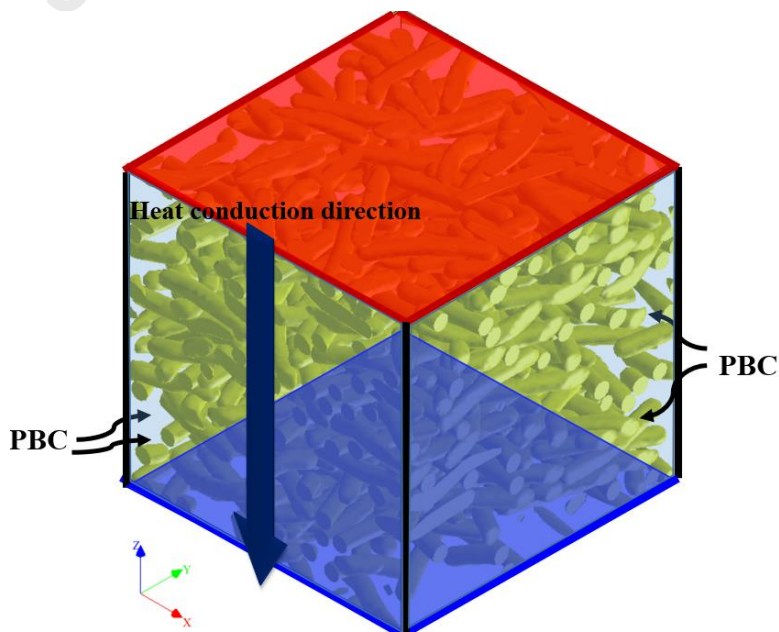
385 in the perpendicular direction in order to compare the numerical results with the experimental
 386 measurements. A tetrahedral mesh was used in simulations because of its flexibility in
 387 modelling complex 3D geometries (Fig. 19). The effective thermal conductivity (λ_{eff}) is
 388 calculated as:

$$\lambda_{eff} = \frac{q_h}{\Delta T} \quad (1)$$

390 where q_h is volume-averaged heat flux in the RVE along the Z-direction and ΔT is the
 391 imposed temperature difference.
 392

Constituents	Thermal conductivity (W/m.K)
Matrix of C1-composite	0.168
Matrix of C2-composite	0.143
Straw	0.051
Air	0.026

393 **Tab. 5.** Thermal conductivities of constituents

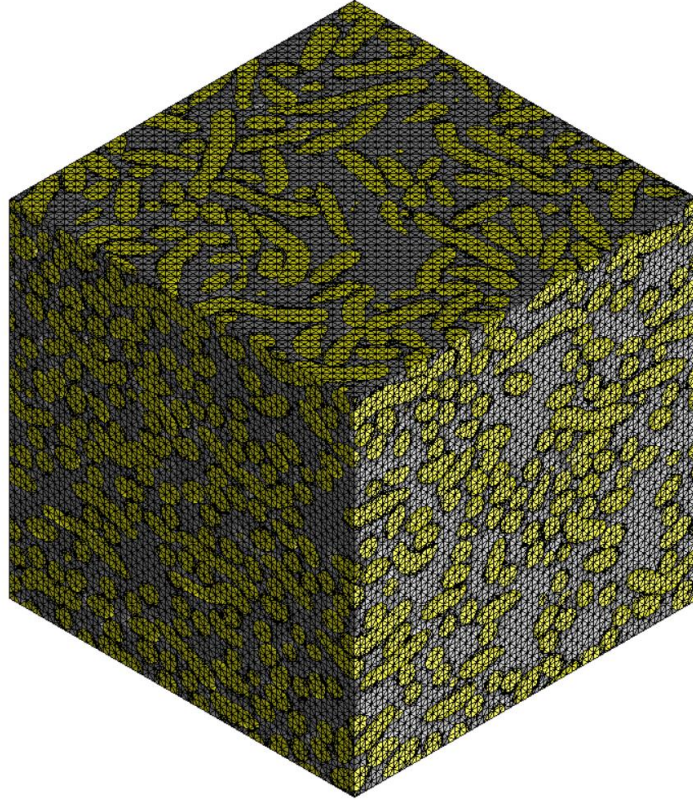


395

396

397 **Fig. 18.** Direction of thermal conduction between hot and cold sides and periodic boundary
398 conditions (PBC) imposed on the other faces.

399



400

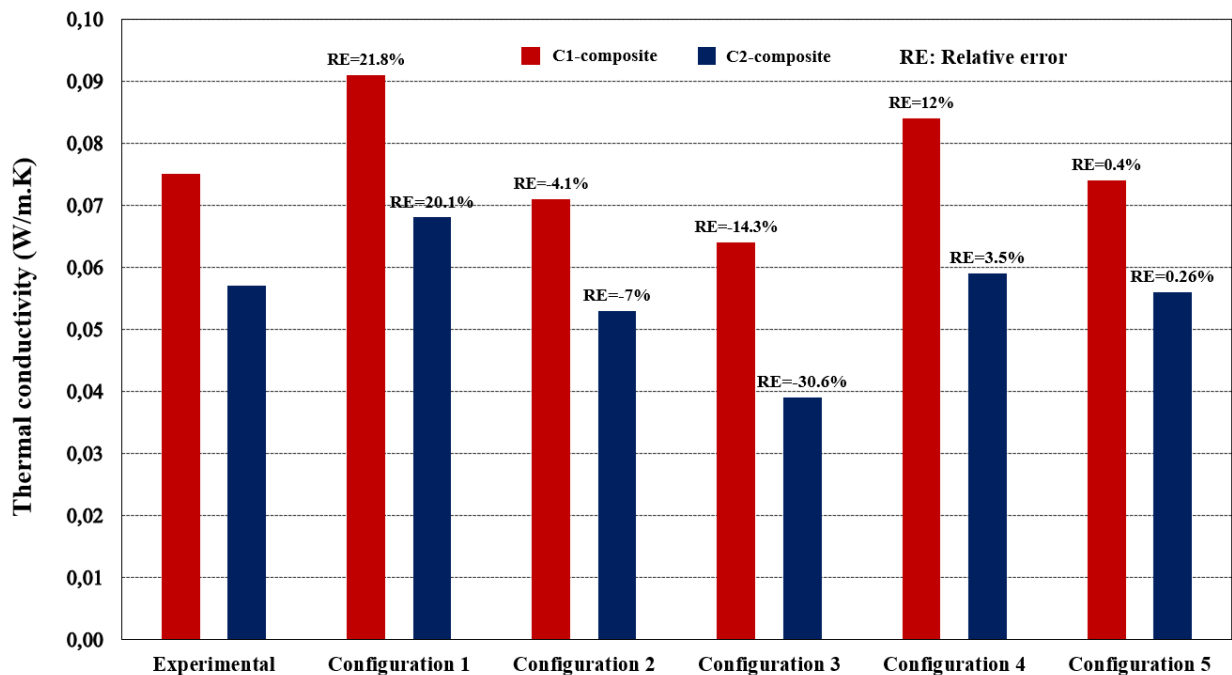
401 **Fig. 19.** Three-dimensional mesh of the RVE using tetrahedral elements.

402 Fig. 20 shows the results obtained in the different configurations presented above. It appears
403 that the classical representation of the microstructure by inclusions embedded in a matrix with
404 perfect interface between the matrix and the inclusion, provides results is far away from those
405 obtained experimentally with an error of about 20% for the two biocomposites.

406 The microstructure adopted in the second configuration has improved the obtained numerical
407 results. Indeed, the numerical values are close to those obtained experimentally, the relative
408 errors are of the order of 4.13% and 7.03%, respectively for the composite with a high and
409 low binder content. Moreover, the third proposed configuration by introducing coated fibers
410 in a void volume has largely underestimated the thermal conductivity of the materials with an
411 error of up 30 % for the C2 biocomposite. However, the replacement of this matrix (void) by

412 a porous matrix allowed satisfactory results, particularly for the low-dosage composite C2.
 413 Finally, considering another phase between the binder and the matrix allowed to reproduce
 414 faithfully the experimental results in the case of both composites.

415 We can confirm from these results the significant impact of the choice of microstructure on
 416 the estimation of the effective thermal conductivity of materials. Indeed, although the volume
 417 fractions of the three phases of the material are the same in the five configurations considered,
 418 the results were very variable. This result confirms that the effective properties of
 419 heterogeneous material depend not only on the properties of the constituents but also on their
 420 interactions represented by the different conceptual models of the microstructure. Therefore,
 421 choosing a microstructure close to that of the real material is an essential step to be able to
 422 accurately predict the effective thermal conductivity.



423

424 **Fig. 20.** Comparison between experimental and modelled thermal conductivities.

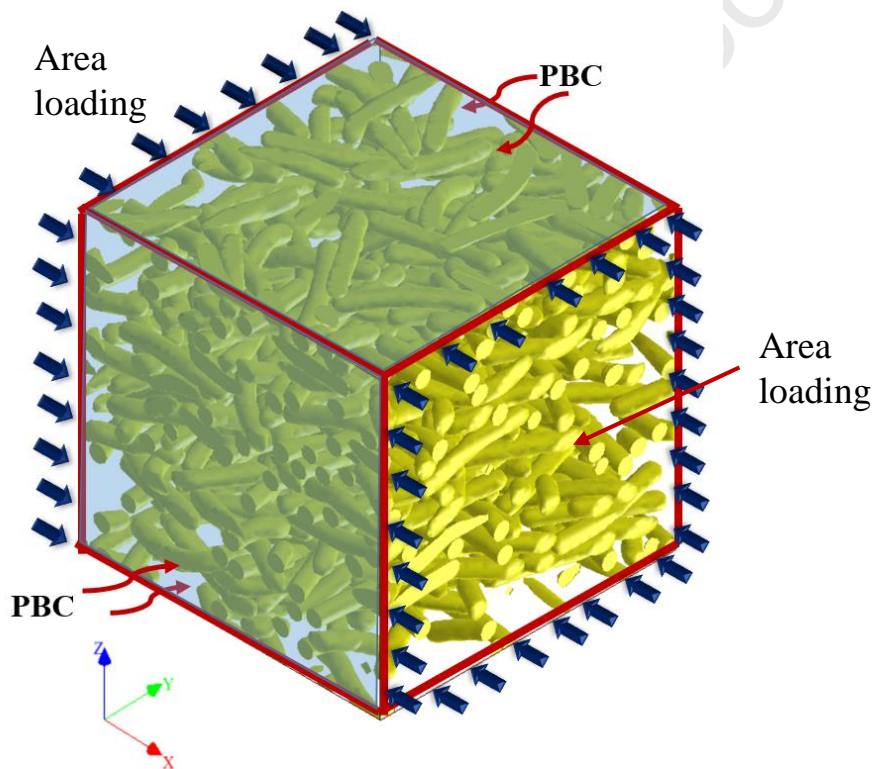
425

426 3.4 Modeling of the nonlinear mechanical behavior

427

428 Numerical homogenization was also used to reproduce the mechanical behavior of the two
 429 studied straw composites. As well as the problem of heat conduction, a representative volume
 430 element is considered, which consists of elastic heterogeneities and an elastoplastic matrix.
 431 Two shapes of inclusion were adopted, spherical representing the porosity (inter-granular and
 432 tubular pore of straw) and curved sphero-cylindrical corresponding to the vegetable fibres.
 433 The boundary and loading conditions were imposed on the surfaces as shown in the Fig. 21.

434



435

436 **Fig. 21.** Direction of mechanical loading and periodic boundary conditions (PBC) imposed on
 437 the other faces.

438 Tab. 6 gives

the elastic

439 properties of

the inclusions

440 used in the

simulations.

	Straw	Air void
Young's modulus E (MPa)	0.2	10^{-6}
Poisson's ratio ν	0.1	0.001

441

442

443

Tab.6 . Elastic parameters of the inclusions (Straw + air)444 The behavior of the matrix is described by a J_2 -plasticity model with nonlinear isotropic445 hardening. This model is based on the Von Mises equivalent stress σ_{eq} defined as :

$$\sigma_{eq} = \sqrt{J_2(\boldsymbol{\sigma})} = \sqrt{\frac{3}{2}(\mathbf{s}:\mathbf{s})} \quad (2)$$

446 where $J_2(\boldsymbol{\sigma})$ is the second invariant of the deviatoric stress tensor \mathbf{s} , and is expressed as:

$$\begin{aligned} J_2(\boldsymbol{\sigma}) &= \frac{3}{2}(\mathbf{s}:\mathbf{s}) \\ &= \frac{2}{3} \left[\left(\boldsymbol{\sigma} - \frac{1}{3} Tr(\boldsymbol{\sigma}) \mathbf{I} \right) : \left(\boldsymbol{\sigma} - \frac{1}{3} Tr(\boldsymbol{\sigma}) \mathbf{I} \right) \right] \\ &= \frac{1}{2} [(\sigma_{11} - \sigma_{22})^2 + (\sigma_{22} - \sigma_{33})^2 + (\sigma_{33} - \sigma_{11})^2] + 3[(\sigma_{12}^2 + \sigma_{23}^2 + \sigma_{31}^2)] \end{aligned} \quad (3)$$

447 In this constitutive model, the response is assumed to be linear elastic as long as the following

448 condition is satisfied:

$$\sigma_{eq} \leq \sigma_Y \quad (4)$$

449 where σ_Y is the initial yield stress.

450 The total strain is assumed to be the sum of the plastic strain and elastic strain:

$$\boldsymbol{\epsilon} = \boldsymbol{\epsilon}^e + \boldsymbol{\epsilon}^p \quad (5)$$

451 The Cauchy stress and the elastic strain are then related by :

$$\boldsymbol{\sigma} = \underline{\underline{\mathbf{C}}}: (\boldsymbol{\epsilon} - \boldsymbol{\epsilon}^p) \quad (6)$$

452 where $\underline{\underline{\mathbf{C}}}$ is Hooke's operator. When σ_{eq} exceeds σ_Y , the response becomes nonlinear and

453 plastic deformation appears. In this case, the Cauchy stress is given by

$$\sigma_{eq} = \sigma_Y + R(p) \quad (7)$$

454 where $R(p)$ is the hardening stress expressed by a exponential and linear law:

$$R(p) = kp + \sigma_{\infty}[1 - \exp(-mp)] \quad (8)$$

455 Where k : is a linear hardening modulus, σ_{∞} : is a hardening modulus, m : is a hardening
456 exponent and p the accumulated plastic strain, expressed as,

$$p(t) = \int_0^t \dot{p}(\tau) \, d\tau \quad (9)$$

457 With

$$\dot{\mathbf{p}} = \frac{2}{3} \sqrt{J_2(\dot{\boldsymbol{\epsilon}}^p)} = \sqrt{\frac{2}{3} \dot{\boldsymbol{\epsilon}}^p : \dot{\boldsymbol{\epsilon}}^p} \quad (10)$$

458 A yield function $f(\sigma, R)$ can be defined,

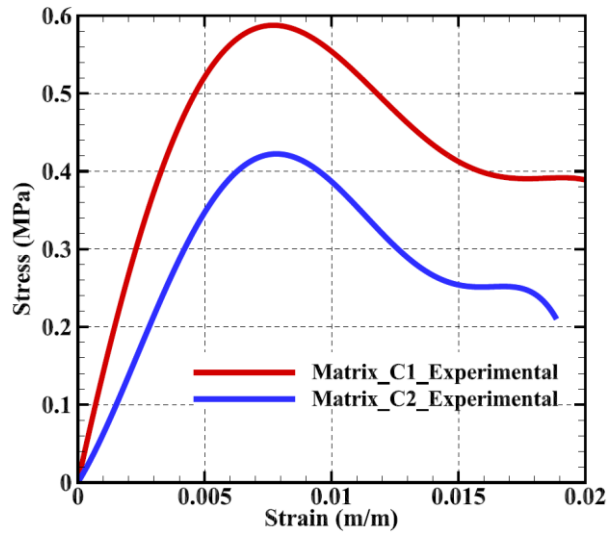
$$f(\sigma, R) = \sigma_{\text{eq}} - \sigma_Y - R(p) \leq 0 \quad (11)$$

459 If $f(\sigma, R) \leq 0$, the material evolves in the elastic domain. Otherwise it is in the plastic region.

460 The evolution of the plastic strain tensor $\boldsymbol{\epsilon}^p$ is given by the normality rule :

$$\dot{\boldsymbol{\epsilon}}^p = \dot{\mathbf{p}} \frac{\partial f}{\partial \sigma} \quad (12)$$

461 To determine the parameters ($\sigma_Y, \sigma_{\infty}, k, m$) of the micromechanical model, uniaxial
462 compression tests were carried out on binder pastes for each case, Fig. 22 illustrates the stress-
463 strain curves obtained for the two matrices and Tab. 7 shows the parameters identified from
464 these curves.



465

466

Fig. 22. Mechanical behavior of pure binders

467

	Matrix_C1	Matrix_C2
Poisson's ratio ν	0.3	0.3
Young's modulus E(MPa)	100	85
Limite d'élasticité σ_Y (MPa)	0.25	0.09
Hardening modulus σ_∞ (MPa)	0.38	0.37
Hardening exponent m (MPa)	1400	1396
Linear hardening modulus k (MPa)	-5.5	-3.8

468

Tab. 7 Parameters used for the mechanical modelling

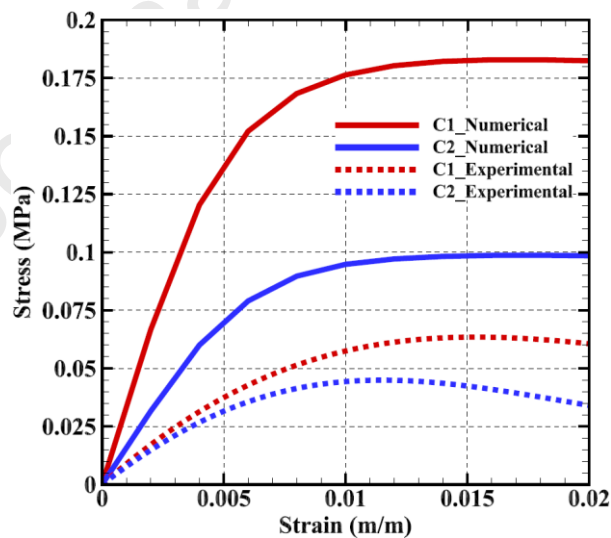
469

470 The mechanical behavior of the two composites was estimated by following the steps of
471 configuration 1 (Fig. 11). First, the spherical inclusions and the matrix were homogenized.

472 Then, in a second step, the curved fibers were integrated in the equivalent medium determined
473 in the first step and a new homogenization is performed to obtain the effective mechanical
474 behavior of the composite. The simulations were carried out by imposing on one face of the
475 RVE a uniaxial deformation (in the x-direction, Fig. 21) and periodic conditions in the other
476 faces. A tetrahedral mesh was also used here in both calculation steps.

477 Fig. 23 compares the experimental stress-strain curves with those predicted by the numerical
478 homogenization. The numerical curves are well above the experimental ones in both the

479 elastic and plastic region. This discrepancy can be associated with the matrix input data,
 480 evaluated from the compression tests on binder pastes alone. In other words, the behaviour of
 481 pure binders may be different from that of binders mixed with fibres, leading to significant
 482 errors. The binder alone has a compactness that is totally different in the presence of
 483 aggregates. This problem was also discussed by Akkaoui et al. 2017 [28]. Indeed, to
 484 determine the elastic properties of the constituent phases of wood concrete, the authors carried
 485 out a calibration of the developed model on the experimental results of the composite. They
 486 noticed that the calibrated modulus are lower than those measured on the pure binder paste.
 487 This difference is due to the interactions between the plant fibers and the binder. The presence
 488 of the fibers strongly impacts the hydration and drying process of the binder [42–44]. In
 489 addition, the cracks that appear in certain area of the fiber-matrix interfaces lead to additional
 490 porosity which can also be the cause of the weakness of the calibrated properties for the
 491 binder.



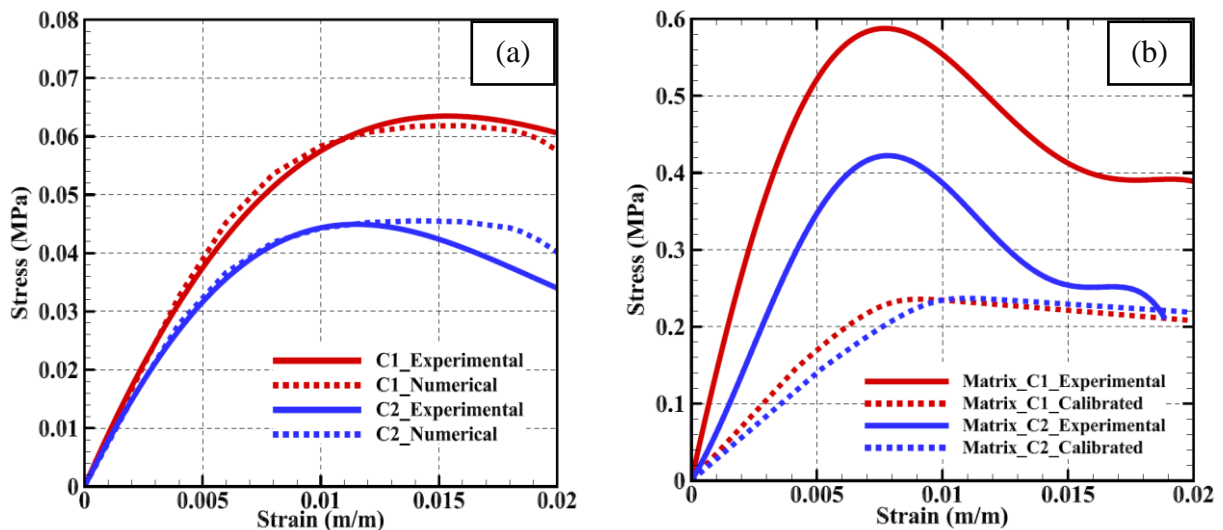
492
 493 **Fig. 23.** Modeled and experimental mechanical behavior of the two composites

494 Therefore, we propose to determine the behavior of the matrix using an inverse analysis based
 495 on numerical homogenization. For this, we assume the following hypotheses: (i) The
 496 representative volume element is cubic with an edge equal to 3 cm (ii) Vegetable fibers have a
 497 curved spherocylindrical shape, randomly oriented in the plane and they have the same

498 aspect ratio (iii) Porosity has a spherical shape (iv) The behavior of the inclusions is elastic as
 499 shown in the Tab. 8. (v) The behavior of the matrix is elastoplastic. The macroscopic stresses
 500 and strains are calculated from the mean relations of the local stresses and strains of the RVE.
 501 We aim to evaluate the properties of the matrix (parameters of J2-plasticity model). In a first
 502 step, we determine the elastic properties of the matrix allowing to minimize the difference
 503 between the experimental and numerical curve by using least squares. Once this condition is
 504 satisfied, we fix the elastic parameters and we proceed to determine the plastic parameters
 505 ($\sigma_Y, \sigma_\infty, k, m$) of the J2-plasticity model using the same algorithm.

506 Fig. 24(a) shows a good agreement between the effective behavior and that obtained from the
 507 experimental tests, whether for the composite with high or low binder content. In fact, the
 508 Young's modulus and the estimated mechanical strengths are very close to the experimental
 509 values, the standard deviation does not exceed 3%. Fig. 24(b) shows the stress-strain curves
 510 deduced from the compression tests on pure binders and those obtained by inverse analysis.
 511 This result confirms the major impact of plant fibres on the reduction of the mechanical
 512 properties of the matrices.

513 The approach proposed in this study can be used to orient the formulations of studied
 514 materials by proposing composites suitable for each use with a well-defined criterion.



515 **Fig. 24.** Calibrated and experimental mechanical behavior (a) composites (b) matrices

	Matrix_C1	Matrix_C2
Poisson's ratio ν	0.3	0.3
Young's modulus E(MPa)	30	35
Limite d'élasticité σ_Y (MPa)	0.15	0.145
Hardening modulus σ_∞ (MPa)	0.098	0.097
Hardening exponent m (MPa)	1800	1795
Linear hardening modulus k (MPa)	-2.9	-2.5

516 **Tab. 8** Parameters used for the modeling of the mechanical behavior

517 **4 Model application and discussion**

518

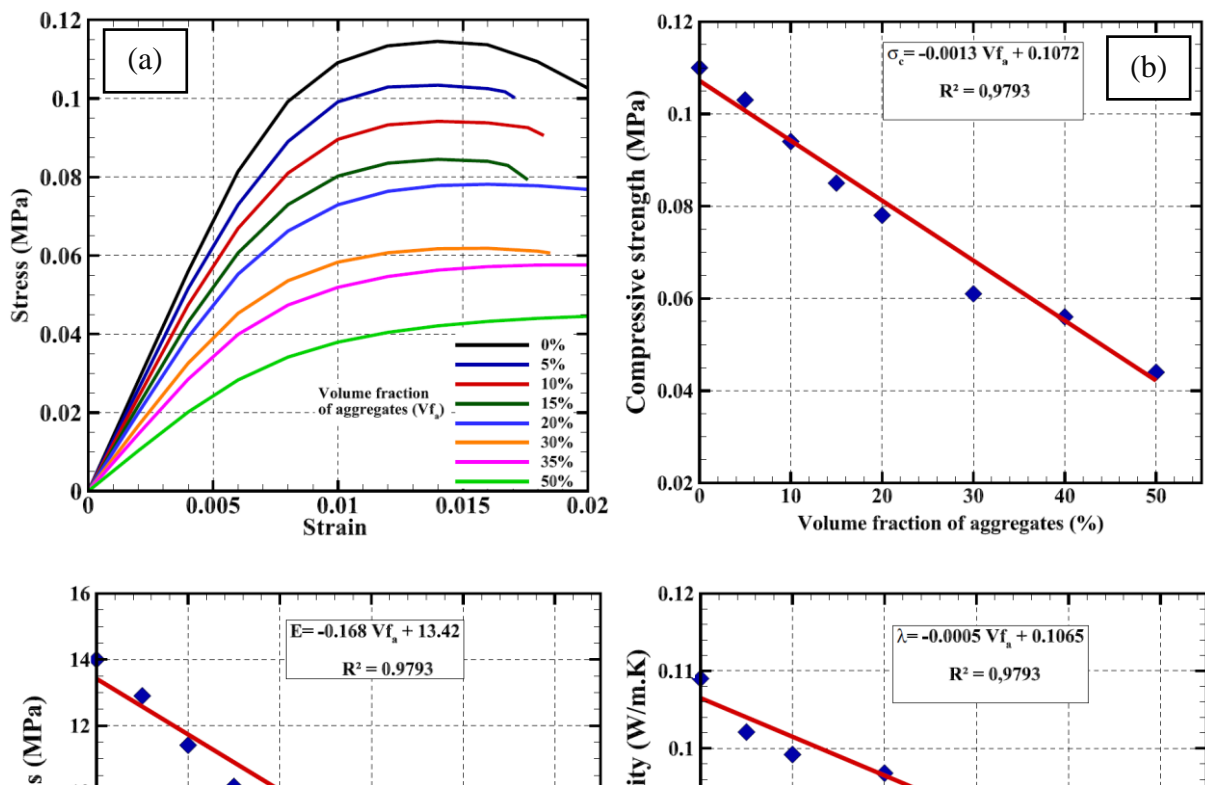
519 As previously mentioned in the state of the art section, the characterization of biobased
 520 materials, has shown that their macroscopic properties are closely related to the
 521 manufacturing parameters, such as, the nature and fraction of the binder, the nature and
 522 fraction of the aggregates, the size of the aggregates, and the casting process (compaction)
 523 which strongly influences the orientation of the aggregates. Other works in the literature have
 524 also shown the great sensitivity of the thermal conductivity to moisture content of the material
 525 [22–24].

526 The numerical model proposed in this work represents a good tool which could be used to
 527 optimize the properties of these materials as a function of physical properties of the
 528 components and microstructural description.

529 Among the manufacturing parameters of biocomposites that this proposed modelling will be
 530 able to give is the proportions of components or component volume fraction of the binder, the
 531 aggregates and the porosity. Fig. 25 shows an example of the results obtained by the model on
 532 the variation of thermal and mechanical properties of C1-composite as a function of volume
 533 fraction of the aggregates (Vfa).

534 Numerical simulations were performed using the microstructure described in configuration 1
 535 (Fig. 11). In the first step, the binder and porosity were homogenized and in the second step
 536 several volume fractions (between 5% and 50%) of the aggregates were tested and

537 homogenized. These simulations were carried out using the VERs and the boundary
 538 conditions presented previously in the figures 18 and 21. Fig.25-a shows the variation of the
 539 mechanical behavior of the composite as a function of the volume fraction of the aggregates.
 540 It is clear that the stress strain curves become more ductile with the increase in volume
 541 fraction of the aggregates. As expected, the more this fraction of the aggregates decreases, the
 542 more the behavior of the composite becomes close to that of the matrix. Similar results were
 543 obtained by Arnaud et al. 2012 [21] for the hemp concrete. Moreover, as displayed in Fig. 25-
 544 b and 25-c, a quasi-linear correlations were found between the mechanical properties and the
 545 volume fraction of the aggregates. The compressive strength and Young's modulus decrease
 546 proportionally with increasing percentage of aggregates. These results are in agreement with
 547 the results found by Akkaoui.2015 [45] for wood-aggregate concrete, Mazhoud et al. 2017
 548 [46] for hemp clay composite, and Pham 2014 [27] for hemp concrete. Fig. 25-d also shows a
 549 quasi-linear evolution between the thermal conductivity and the volume fraction of the
 550 aggregates. As known, the increase in percentage of aggregates leads to a decrease in thermal
 551 conductivity. The same trend was obtained also by Cerezo.2005 [25], Tran-Le et al. 2018 [29]
 552 and Pham.2014 [27] that used analytical models to predict the thermal conductivity of hemp
 553 concrete.



563
564
565
566
567
568
569
570
571

572 **Fig. 25.** Variation of mechanical and thermal properties as a function of volume fraction of
573 the aggregates (Vf_a) (a) nonlinear mechanical behavior (b) Compressive strength (c) Young
574 modulus (d) thermal conductivity

575

576 The use of the modelling approach presented here can make it possible to propose optimal
577 mixtures with an attractive thermal and mechanical properties depending on the final
578 applications and the criteria for use in buildings. The numerical modelling is able to predict
579 the stress-strain curve of the materials and to estimate their mechanical strength even for high
580 fraction of aggregate unlike analytical models used in literature which are limited only to
581 fractions not exceeding 30 %. Despite the advantage of this promising modelling method that
582 allows to study complex microstructures, the proposed methodology is based on some
583 assumptions that affect certain results. The first, is that the mechanical properties of the
584 binder is determined by inverse analysis assuming that the volume fraction of the aggregates
585 in composite is constant. The variation of aggregate fraction can impact significantly the
586 intrinsic characteristics of the matrix due to the interactions between the plant aggregates and
587 the binder as we previously stated. Therefore, it will be interesting to evaluate the influence of
588 plant aggregates on the intrinsic properties of the matrix. Moreover, the aggregate-matrix
589 interface is assumed to be perfect. This assumption is not realistic as it has been shown by the
590 microscopic observation. The experimental characterization of this interface and its

591 consideration in the material modelling in terms of thickness and properties has not yet
592 reached a complete consensus, and remains an important point of investigation.

593

594 **5 Conclusion**

595

596 The purpose of this paper was to model the thermal and mechanical behavior of two types of
597 straw biocomposites. Given the limitations of the analytical methods in taking into account all
598 microstructure characteristics influencing the behavior of biobased materials, a numerical
599 homogenization was adopted in this work to model their complex behavior. First, a detailed
600 description of morphology, size and spatial distribution of inclusions was carried out. The X-
601 ray microtomography is used to determine the volume fractions of the different phases of the
602 bio-based materials. Then, a statistical approach based on the convergence of the apparent
603 properties was applied to determine the size of the representative volume element. The results
604 showed that the RVE size depends on the fraction of inclusions in the case of mechanical or
605 thermal loading. Subsequently, the effective conductivity and the non-linear behavior of the
606 composites were modeled. In the case of thermal conductivity, five configurations were
607 proposed to show the effect of microstructure on the prediction of the effective properties.
608 The obtained results have shown that the classical representation of materials by
609 heterogeneities embedded in a matrix is inappropriate for the complex materials of this study
610 contrary to the classical polymer or metallic composites with a low ratio of fibers. The
611 compressive mechanical behavior was first modeled using as input data for the matrix, the
612 parameters determined from the experimental tests on the pure binders. This led to a large
613 overestimation of the mechanical behavior. Therefore, a calibration of the numerical model
614 with the experimental curves of the composites was necessary to access the properties of the
615 matrices. The results showed that the properties determined from the experimental curves of
616 pure binders are much lower than those identified, by inverse analysis, from the curves of the

617 composites. These results confirm the need to consider the fiber-matrix interaction in the
 618 numerical model to accurately predict the mechanical behavior of biobased composites.
 619 However, the approach proposed in this work remains useful to guide the optimization of the
 620 mixtures design of the biocomposite materials.

621 **6 Acknowledgements**

622 The authors gratefully acknowledge the “REGION CENTRE” for the financial support of the
 623 research program PEPITE.

624 **7 References**

- 625 [1] S. Amziane, F. Collet, Bio-aggregates based building materials : State-of-the-Art Report
 626 of the RILEM Technical Committee 236-BBM, Springer, 2017. ISBN 9402410317
- 627 [2] N. Belayachi, M. Bouasker, D. Hoxha, M. Al-Mukhtar, Thermo-Mechanical Behaviour
 628 of an Innovant Straw Lime Composite for Thermal Insulation Applications, AMM. 390
 629 (2013) 542–546. <https://doi.org/10.4028/www.scientific.net/AMM.390.542>.
- 630 [3] N. Belayachi, D. Hoxha, M. Slaimia, Impact of accelerated climatic aging on the
 631 behavior of gypsum plaster-straw material for building thermal insulation, Construction
 632 and Building Materials. 125 (2016) 912–918.
 633 <https://doi.org/10.1016/j.conbuildmat.2016.08.120>.
- 634 [4] M.P. Sáez-Pérez, M. Brümmer, J.A. Durán-Suárez, A review of the factors affecting the
 635 properties and performance of hemp aggregate concretes, Journal of Building
 636 Engineering. 31 (2020) 101323. <https://doi.org/10.1016/j.job.2020.101323>.
- 637 [5] Y. Jiang, A. Phelipot-Mardele, F. Collet, C. Lanos, M. Lemke, M. Ansell, A. Hussain,
 638 M. Lawrence, Moisture buffer, fire resistance and insulation potential of novel bio-clay
 639 plaster, Construction and Building Materials. 244 (2020) 118353.
 640 <https://doi.org/10.1016/j.conbuildmat.2020.118353>.
- 641 [6] T. Jami, S.R. Karade, L.P. Singh, A review of the properties of hemp concrete for green
 642 building applications, Journal of Cleaner Production. 239 (2019) 117852.
 643 <https://doi.org/10.1016/j.jclepro.2019.117852>.
- 644 [7] M.Viel, Développement de composites bio-sourcés destinés à l’isolation des bâtiments
 645 (Ph.D.thesis) Université Rennes 1. 2018
- 646 [8] P. Tronet, T. Lecompte, V. Picandet, C. Baley, Study of lime hemp concrete (LHC) –
 647 Mix design, casting process and mechanical behaviour, Cement and Concrete
 648 Composites. 67 (2016) 60–72. <https://doi.org/10.1016/j.cemconcomp.2015.12.004>.
- 649 [9] B. Mazhoud, F. Collet, S. Pretot, J. Chamoin, Hygric and thermal properties of hemp-
 650 lime plasters, Building and Environment. 96 (2016) 206–216.
 651 <https://doi.org/10.1016/j.buildenv.2015.11.013>.
- 652 [10] A. Shea, M. Lawrence, P. Walker, Hygrothermal performance of an experimental hemp-
 653 lime building, Construction and Building Materials. 36 (2012) 270–275.
 654 <https://doi.org/10.1016/j.conbuildmat.2012.04.123>.

- 655 [11] O. Kinnane, A. Reilly, J. Grimes, S. Pavia, R. Walker, Acoustic absorption of hemp-lime
656 construction, *Construction and Building Materials*. 122 (2016) 674–682.
657 <https://doi.org/10.1016/j.conbuildmat.2016.06.106>.
- 658 [12] P. Glé, E. Gourdon, L. Arnaud, Acoustical properties of materials made of vegetable
659 particles with several scales of porosity, *Applied Acoustics*. (2011) 11.
- 660 [13] S. Elfordy, F. Lucas, F. Tancret, Y. Scudeller, L. Goudet, Mechanical and thermal
661 properties of lime and hemp concrete (“hempcrete”) manufactured by a projection
662 process, *Construction and Building Materials*. 22 (2008) 2116–2123.
663 <https://doi.org/10.1016/j.conbuildmat.2007.07.016>.
- 664 [14] S. Benfratello, C. Capitano, G. Peri, G. Rizzo, G. Scaccianoce, G. Sorrentino, Thermal
665 and structural properties of a hemp–lime biocomposite, *Construction and Building*
666 *Materials*. 48 (2013) 745–754. <https://doi.org/10.1016/j.conbuildmat.2013.07.096>.
- 667 [15] Y. Florentin, D. Pearlmutter, B. Givoni, E. Gal, A life-cycle energy and carbon analysis
668 of hemp-lime bio-composite building materials, *Energy and Buildings*. 156 (2017) 293–
669 305. <https://doi.org/10.1016/j.enbuild.2017.09.097>.
- 670 [16] B. Seng, C. Magniont, S. Lorente, Characterization of a precast hemp concrete. Part I:
671 Physical and thermal properties, *Journal of Building Engineering*. 24 (2019) 100540.
672 <https://doi.org/10.1016/j.jobe.2018.07.016>.
- 673 [17] C. Maalouf, C. Ingraio, F. Scrucca, T. Moussa, A. Bourdot, C. Tricase, A. Presciutti, F.
674 Asdrubali, An energy and carbon footprint assessment upon the usage of hemp-lime
675 concrete and recycled-PET façades for office facilities in France and Italy, *Journal of*
676 *Cleaner Production*. 170 (2018) 1640–1653.
677 <https://doi.org/10.1016/j.jclepro.2016.10.111>.
- 678 [18] R. Haik, G. Bar-Nes, A. Peled, I.A. Meir, Alternative unfired binders as lime
679 replacement in hemp concrete, *Construction and Building Materials*. 241 (2020) 117981.
680 <https://doi.org/10.1016/j.conbuildmat.2019.117981>.
- 681 [19] F. Delhomme, A. Hajimohammadi, A. Almeida, C. Jiang, D. Moreau, Y. Gan, X. Wang,
682 A. Castel, Physical properties of Australian hurd used as aggregate for hemp concrete,
683 *Materials Today Communications*. 24 (2020) 100986.
684 <https://doi.org/10.1016/j.mtcomm.2020.100986>.
- 685 [20] F. Collet, S. Pretot, B. Mazhoud, L. Bessette, C. Lanos, R.A. Bergès, Comparing hemp
686 composites made with mineral or organic binder on thermal, hygric and mechanical
687 point of view, *Academic Journal of Civil Engineering*, 33(2015), 228-234.
- 688 [21] L. Arnaud, E. Gourlay, Experimental study of parameters influencing mechanical
689 properties of hemp concretes, *Construction and Building Materials*. 28 (2012) 50–56.
690 <https://doi.org/10.1016/j.conbuildmat.2011.07.052>.
- 691 [22] D. Taoukil, A. El bouardi, F. Sick, A. Mimet, H. Ezbakhe, T. Ajzoul, Moisture content
692 influence on the thermal conductivity and diffusivity of wood–concrete composite,
693 *Construction and Building Materials*. 48 (2013) 104–115.
694 <https://doi.org/10.1016/j.conbuildmat.2013.06.067>.
- 695 [23] E. Gourlay, P. Glé, S. Marceau, C. Foy, S. Moscardelli, Effect of water content on the
696 acoustical and thermal properties of hemp concretes, *Construction and Building*
697 *Materials*. 139 (2017) 513–523. <https://doi.org/10.1016/j.conbuildmat.2016.11.018>.
- 698 [24] F. Collet, S. Pretot, Thermal conductivity of hemp concretes: Variation with
699 formulation, density and water content, *Construction and Building Materials*. 65 (2014)
700 612–619. <https://doi.org/10.1016/j.conbuildmat.2014.05.039>.
- 701 [25] C. Véronique, Propriétés mécaniques, thermiques et acoustiques d’un matériau à base de
702 particules végétales : approche expérimentale et modélisation théorique, (Ph.D.
703 thesis), Institut National des Sciences Appliquées de Lyon, 2005.

- 704 [26] N.E. Hajj. Contribution à la conception et à l'élaboration d'une âme multicouche
705 multifonctionnelle agrosourcée pour panneau sandwich : étude expérimentale et
706 modélisation. PhD thesis, Université de Picardie Jules Verne, 2010.
- 707 [27] TH Pham. Modélisation multi-échelles des propriétés thermiques et élastiques de
708 composites chaux-chanvre. PhD thesis, Université de Bretagne-Sud, 2014.
- 709 [28] A. Akkaoui, S. Caré, M. Vandamme, Experimental and micromechanical analysis of the
710 elastic properties of wood-aggregate concrete, *Construction and Building Materials*. 134
711 (2017) 346–357. <https://doi.org/10.1016/j.conbuildmat.2016.12.084>.
- 712 [29] A.D. Tran-Le, S.-T. Nguyen, T. Langlet, A novel anisotropic analytical model for
713 effective thermal conductivity tensor of dry lime-hemp concrete with preferred spatial
714 distributions, *Energy and Buildings*. 182 (2019) 75–87.
715 <https://doi.org/10.1016/j.enbuild.2018.09.043>.
- 716 [30] A. Couture, V. François, J.C. Cuillère, P. Pilvin, Modélisation de la microstructure de
717 composites particulaires : Application à l'homogénéisation en conduction thermique,
718 13e colloque national en calcul des structures, 2017
- 719 [31] S. Mom, S Dartois, A. Ben Hamida, H. Dumontet, and H. Boussa. Modélisation itérative
720 multi-échelles du béton de chanvre. In *Congrès français de mécanique*, 2011.
- 721 [32] T. Nguyen-Sy, A.D. Tran-Le, T. Nguyen-Thoi, T. Langlet, A multi-scale
722 homogenization approach for the effective thermal conductivity of dry lime–hemp
723 concrete, *Journal of Building Performance Simulation*. 11 (2018) 179–189.
724 <https://doi.org/10.1080/19401493.2017.1323009>.
- 725 [33] Z.K. Low, N. Blal, N. Naouar, D. Baillis, Influence of boundary conditions on
726 computation of the effective thermal conductivity of foams, *International Journal of Heat
727 and Mass Transfer*. 155 (2020) 119781.
728 <https://doi.org/10.1016/j.ijheatmasstransfer.2020.119781>.
- 729 [34] K. Miled, O. Limam, Effective thermal conductivity of foam concretes: Homogenization
730 schemes vs experimental data and FEM simulations, *Mechanics Research
731 Communications*. 76 (2016) 96–100. <https://doi.org/10.1016/j.mechrescom.2016.07.004>.
- 732 [35] B. Ismail, N. Belayachi, D. Hoxha, Optimizing performance of insulation materials
733 based on wheat straw, lime and gypsum plaster composites using natural additives,
734 *Construction and Building Materials*. 254 (2020) 118959.
735 <https://doi.org/10.1016/j.conbuildmat.2020.118959>.
- 736 [36] S. Amziane, L. Arnaud, Les bétons de granulats d'origine végétale. Application au béton
737 de chanvre, Lavoisier, 2013.
- 738 [37] R. Hill, Elastic properties of reinforced solids: Some theoretical principles, *Journal of the
739 Mechanics and Physics of Solids*. 11 (1963) 357–372. [https://doi.org/10.1016/0022-5096\(63\)90036-X](https://doi.org/10.1016/0022-5096(63)90036-X).
- 740 [38] Z. Hashin., Analysis of composite materials—a survey. *Journal of applied mechanics*,
741 50(3) :481–505, 1983..
- 742 [39] T. Kanit, S. Forest, I. Galliet, V. Mounoury, D. Jeulin, Determination of the size of the
743 representative volume element for random composites: statistical and numerical
744 approach, *International Journal of Solids and Structures*. 40 (2003) 3647–3679.
745 [https://doi.org/10.1016/S0020-7683\(03\)00143-4](https://doi.org/10.1016/S0020-7683(03)00143-4).
- 746 [40] I.M. Gitman, H. Askes, L.J. Sluys, Representative volume: Existence and size
747 determination, *Engineering Fracture Mechanics*. 74 (2007) 2518–2534.
748 <https://doi.org/10.1016/j.engfracmech.2006.12.021>.
- 749 [41] C. Pelissou, J. Baccou, Y. Monerie, F. Perales, Determination of the size of the
750 representative volume element for random quasi-brittle composites, *International Journal
751 of Solids and Structures*. 46 (2009) 2842–2855.
752 <https://doi.org/10.1016/j.ijsolstr.2009.03.015>.
- 753

- 754 [42] M. Merzoud and MF. Habita. Elaboration de composite cimentaire à base de diss
755 «ampelodesma mauritanica». *Afrique Science : Revue Internationale Des Sciences Et*
756 *Technologie*, 4(2), 2008, (n.d.).
- 757 [43] A. Sellami, M. Merzoud, and S. Amziane. Improvement of mechanical properties of
758 green concrete by treatment of the vegetals fibers. *Construction and Building Materials*,
759 47 :1117–1124, 2013., (n.d.).
- 760 [44] G. Delannoy, S. Marceau, P. Glé, E. Gourlay, M. Guéguen-Minerbe, D. Diafi, S.
761 Amziane, F. Farcas, Impact of hemp shiv extractives on hydration of Portland cement,
762 *Construction and Building Materials*. 244 (2020) 118300.
763 <https://doi.org/10.1016/j.conbuildmat.2020.118300>.
- 764 [45] A. Akkaoui, Bétons de granulats de bois: étude expérimentale et théorique des propriétés
765 thermo-hydro-mécaniques par des approches multi-échelles, Ph.D. thesis Université
766 Paris-Est, 2014..
- 767 [46] B. Mazhoud, F. Collet, S. Pretot, C. Lanos, Mechanical properties of hemp-clay and
768 hemp stabilized clay composites, *Construction and Building Materials*. 155 (2017)
769 1126–1137. <https://doi.org/10.1016/j.conbuildmat.2017.08.121>.

771

772

Modelling of thermal conductivity and nonlinear mechanical behavior of straw insulation composite by a numerical homogenization approach

Brahim ISMAIL¹, Naima BELAYACHI¹, Dashnor HOXHA¹, Laurent ARBARET²

¹ Université d'Orléans, INSA Centre Val de Loire, Université de Tours, Laboratoire de Mécanique Gabriel Lamé Polytech Orléans, 8 rue Léonard de Vinci, 45072 Orléans, France

² ISTO, UMR 7327, Université d'Orléans, CNRS, BRGM, 1A rue de la Férellerie, 45071, Orléans, France

Corresponding author :

Naima Belayachi

Tel : 330238492502

Fax : 330238417063

E-mail address : naima.belayachi@univ-orleans.fr

Postal address : Laboratoire LaMé, Polytech'Orléans

8 Rue Léonard De Vinci

45072, Orléans cedex 2, France

Tables

Composites	Binder	Straw/Binder (kg/kg)	Water/Binder (kg/kg)	Density (kg/m ³)
C1	Lime	0.2	1.1	450
C2	Lime+20% gelatin	0.4	1.1	300

Tab. 1. Composite designation and detailed mixture proportions

	C1	C2
Binder	33%	11%
Straw	30%	35%
Porosity (intergranular)	37%	54%

Tab. 2 . Volume fractions of the different phases for the two composites

Composites	Thermal conductivity (λ /W/m.K)	
	Vertical direction	Horizontal direction
C1	0.075 \pm 0.02	0.064 \pm 0.013
C2	0.057 \pm 0.017	0.051 \pm 0.019

Tab.3 . Thermal conductivity of composites in horizontal and vertical direction

	Matrix	Inclusion
Young's modulus E(MPa)	100	0.2
Poisson's ratio ν	0.3	0.1
Thermal conductivity (λ /W/m.K)	0.168	0.051

Tab. 4. Parameters used to determine effective properties.

Constituents	Thermal conductivity (W/m.K)
Matrix of C1-composite	0.168
Matrix of C2-composite	0.143
Straw	0.051
Air	0.026

Tab. 5. Thermal conductivities of constituents

	Straw	Air void
Young's modulus E (MPa)	0.2	10–6
Poisson's ratio ν	0.1	0.001

Tab.6 . Elastic parameters of the inclusions (Straw + air)

	Matrix_C1	Matrix_C2
Poisson's ratio ν	0.3	0.3
Young's modulus E(MPa)	100	85
Limite d'élasticité σ_Y (MPa)	0.25	0.09
Hardening modulus σ_∞ (MPa)	0.38	0.37
Hardening exponent m (MPa)	1400	1396
Linear hardening modulus k (MPa)	-5.5	-3.8

Tab. 7 Parameters used for the mechanical modelling

	Matrix_C1	Matrix_C2
Poisson's ratio ν	0.3	0.3
Young's modulus E(MPa)	30	35
Limite d'élasticité σ_Y (MPa)	0.15	0.145
Hardening modulus σ_∞ (MPa)	0.098	0.097
Hardening exponent m (MPa)	1800	1795
Linear hardening modulus k (MPa)	-2.9	-2.5

Tab. 8 Parameters used for the modeling of the mechanical behavior

Declaration of interests

The authors declare that they have no known competing financial interests or personal relationships that could have appeared to influence the work reported in this paper.

The authors declare the following financial interests/personal relationships which may be considered as potential competing interests:

Journal Pre-proof